THE JOURNAL OF PHYSICAL CHEMISTRY C

Article

Cite This: J. Phys. Chem. C 2019, 123, 27628−27642

pubs.acs.org/JPCC

Studies of Muonium Reactivity with Uncapped Gold Nanoparticles and with Surface-Adsorbed Benzene on These NPs in Porous Silica Hosts

D. G. Fleming,* W. A. MacFarlane, and J. Xiao

TRIUMF and Department of Chemistry, University of British Columbia, Vancouver, British Columbia V6T1Z1, Canada

D. J. Arseneau

TRIUMF, 4004 Wesbrook Mall, Vancouver, British Columbia V6T2A3, Canada

M. H. Dehn and R. F. Kiefl

TRIUMF and Department of Physics, University of British Columbia, Vancouver, British Columbia V6T1Z1, Canada

V. M. Zamarion,† P.-X. Wang, Y. Cao, and M. J. MacLachlan

Department of Chemistry, University of British Columbia, Vancouver, British Columbia V6T1Z1, Canada

M. D. Bridges

Jules Stein Eye Institute University of California, Los Angeles, California 90095, United States

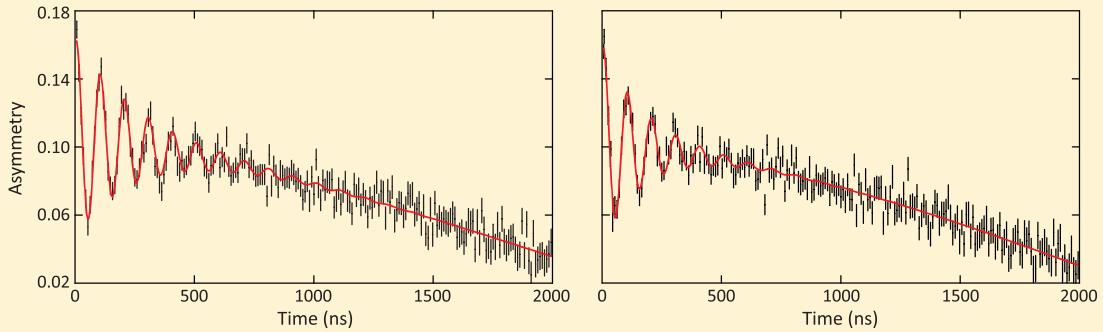

ABSTRACT: Gold nanoparticles (AuNPs) have been a subject of considerable interest in recent years due to both their magnetic and catalytic properties. This paper reports a two-fold study of the reactivity at 300 K of the isotopic hydrogen atom, muonium (Mu = μ^+e^-), (i) with bare *uncapped* AuNPs of different sizes encapsulated in mesoporous (SBA-15) silica hosts, forming a diamagnetic final state in the Mu + AuNP → MuAuNP reaction, and (ii) with surface-adsorbed benzene on these NPs forming the muoniated cyclohexadienyl radical in the Mu + C_6H_6 → Mu$\dot{C}_6H_6$ addition reaction. The measured muon-spin relaxation rates, λ_C, for the chemisorption reaction of Mu with the bare AuNPs show some variation with AuNP size. The Mu + C_6H_6 addition reaction has been studied over a range of benzene loadings both on bare silica and in the AuNP/silica samples. The measured muon-spin relaxation rates, λ_{Tot}, exhibit a linear dependence on benzene concentration over the full range of loadings in both cases, in accord with an Eley−Rideal model of surface reactivity. Rate constants, k_{Bz}, were determined from this dependence which exhibit a 2−3-fold faster reaction rate on the AuNPs than on the bare silica, suggesting a catalytic effect due to benzene adsorbed on these NP surfaces.

1. INTRODUCTION

It is well-known that gold nanoparticles (AuNPs) exhibit important size-dependent catalytic properties.[1−5] In order to study these properties experimentally, it is essential that the NPs remain isolated from one another, which is frequently

Received: September 1, 2019
Revised: October 16, 2019
Published: October 21, 2019

DOI: 10.1021/acs.jpcc.9b08327
J. Phys. Chem. C 2019, 123, 27628−27642

done by "capping" with thiol or other organic groups,[1,6−9] but this changes the nature of the surface and hence the binding of adsorbed molecules, thereby altering their surface reactivity. The AuNPs in the present study were stabilized in mesoporous (SBA-15) silica hosts, which not only prevents their aggregation but also provides an *uncapped* NP surface for reactant molecules to bind to.

Mesoporous silicate materials have received widespread attention of late due to their applications as supports for catalysis, in separation techniques, and in the confinement of guest molecules.[10−12] Siliceous host environments have also generally been important in the realm of heterogeneous catalysis,[13−25] where protonation reactions with guest molecules can form carbocation intermediates[15,23−26] which can then undergo charge neutralization to give neutral H-adduct free radicals. Such radicals can also be formed by direct H atom transfer/addition reactions to unsaturated bonds in these environments,[16,27] a well-known mechanism for hydrogenation reactions in general[3,27] and for the hydrogenation of benzene in particular.[28−31] Though interfacial interactions of this nature are well-known to be important in surface chemistry,[32,33] including for H atom reactivity, there are very few direct measurements of H atom reaction rates in heterogeneous systems, thus providing an important motivation for the present study of the analogue reactions of the muonium atom.

Muonium (Mu = μ^+e^-), with a positive muon as its "nucleus", behaves as the lightest isotope of the hydrogen atom (mass 0.114 amu), and muons are now generally well established as important spin-polarized mass probes in chemistry.[21,34−40] Earlier work on the Mu + C_6H_6 addition reaction in the gas phase[40] is particularly relevant here in comparison with this same reaction on AuNP/silica surfaces.

This paper reports studies of Mu reactivity both with *bare* AuNPs of sizes 8 nm, 10 nm, and 38 nm encapsulated in SBA-15 mesoporous silica, extending an earlier study of a 7 nm NP in a similar environment,[41] and, for the first time, with surface-adsorbed benzene both on bare silica and on the embedded AuNPs in this porous silica environment. The adsorbed benzene (Bz) forms the muoniated cyclohexadienyl radical in the Mu + C_6H_6 → $Mu\dot{C}_6H_6$ addition reaction, previously identified and studied in a variety of different environments,[17,18,21,22] including in AuNP/silica and PtNP/silica samples by Level Crossing Resonance techniques.[42]

Both the pure SBA-15 silica and the AuNP-loaded samples were synthesized by a hydrothermal method developed by Somorjai and co-workers,[19] as adapted in ref 42. The silica grains were micron-sized with mesopores about 7−8 nm in diameter, typical for SBA-15 silica,[19,43,44] with the AuNPs located on the walls of the mesopores.[19] Silica-like environments are also known to produce copious amounts of muonium,[17,42,45] an important consideration here. It is further noted that it is generally difficult to produce H atoms in situ in heterogeneous environments, whereas muonium is easily generated by stopping μ^+ beams therein.

2. SAMPLE PREPARATION AND CHARACTERIZATION

2.1. Preparation. Gold NPs of three different sizes, ∼8 nm, 10 nm, and 38 nm diameter, were synthesized[19,42] and characterized by transmission electron microscopy (TEM), similar to the 7 nm AuNP studied previously.[41] For the small AuNPs, 3.0 g of sodium citrate (99.0%) followed by 6.2 g of polyvinylpyrrolidone (PVP, average MW 10000 Da) were added to 2 L of boiling deionized water, to which 20 mL of a solution containing 0.2 g of chloroauric acid ($HAuCl_4{\cdot}3H_2O$, 99.9% Au) was added; then the solution was boiled for another 15 min, causing a dramatic color change from pale yellow to dark purple. The colloidal solution was concentrated to 100 mL in a rotary evaporator at ∼75 °C. After the solution cooled to room temperature, it was placed in a dialysis bag and dialyzed against deionized water for 2 days to remove excess molecular precursors. Any PVP surfactant that still remained in solution was later removed by calcination in steps of 5 °C up to 500 °C for 5 h. For the larger AuNP, the same procedure was followed but using only 0.14 g of sodium citrate and a solution containing 0.20 g of the Au(III) salt. The smaller amount of citrate added, and a longer reaction time prior to adding the PVP polymer, gives rise to larger NPs, though this size effect can also depend on how the AuNP is stabilized, here by sodium citrate.[2,46]

To synthesize the bare SBA-15 mesoporous silica, typically 6.2 g of Pluronic "P123" template (PEG−PPG-PEG triblock copolymer) was dissolved in 130 mL of DI water and stirred for 15 min at 35 °C. After dissolution, 1.0 mL of 0.5 M sodium fluoride (99%), followed by 9.7 mL of TMOS (tetramethyl orthosilicate, 98%), as a silica source, was added. The colloidal solution turned translucent white and was left to age for 3 days; then it was centrifuged and washed with ethanol and dried at 123 °C for 38 h. The sample was then calcined at ∼500 °C to remove any residual organic template, as monitored by thermogravimetric analysis (TGA), typically yielding 3 g of white silica product. These conditions[43] are expected to yield a highly hydroxylated surface, up to about 8 hydroxyls/nm^2 for mesoporous SBA-15 silica.

It is important to minimize the temperature and duration of the calcination. If the temperature is too high,[47] cracking of the -SiOH bonds in the SBA-15 silica can occur, leading to additional water loss with the formation of "dangling bonds" like −O−Si· or −Si·−, paramagnetic sites that are a possible source of spin relaxation in the μSR studies reported below.

The AuNP-loaded SBA-15 mesoporous samples were prepared by a procedure similar to that for the bare SBA-15 sample, but the colloidal nanoparticle solution was first mixed with the template solution. For a nominal 2.5 wt % loading of AuNPs in the silica, 67.5 mL of the previous gold nanoparticle solution was added to 127 mL of template solution containing 6.2 g of P123; then the reaction mixture was stirred for 45 min and left to equilibrate. For the higher loading, the only difference was in the ratio between the polymer templates and the nanoparticle solutions, with the sequence of reagent addition also having an effect on the AuNP size.[48] Thus, 6.2 g of P123 was dissolved in only 74.5 mL of DI water, while 120 mL of nanoparticle solution was used, giving a final nominal loading of 4.5 wt %. These samples were again calcined, as above, to remove any residual template, also yielding ∼3 g of product, here of a pinkish or orange-like color for the smaller sizes but closer to mauve for the 38 nm size. It is important to emphasize that these AuNPs are *uncapped*, while being kept isolated within the SBA-15 porous silica framework, in contrast to more common practice where this isolation is done via organic capping agents.[1,6−9,46]

2.2. Sample Characterization. Samples were characterized by elemental analysis, thermogravimetric analysis (TGA)−time profiles for the pure silica, by Brunauer, Emmett, Teller (BET) measurements of surface areas for both the bare and AuNP-loaded samples, by powder X-ray diffraction (PXRD), and by both transmission electron microscopy

DOI: 10.1021/acs.jpcc.9b08327
J. Phys. Chem. C 2019, 123, 27628−27642

(TEM) to establish the AuNP sizes and SEM (scanning electron microscopy) to establish the sample morphologies.

The elemental analysis showed trace hydrogen at 1 wt % due to SiOH groups in the silica. TGA profiles of the bare silica samples showed four separate steps of mass loss, as described in the thesis study of ref 42. The AuNP sizes were mainly determined by TEM, compared also with PXRD. For a nominal 8 nm size, TEM images gave a mean value of 8.6 ± 1.6 nm (HWHM), while for the 10 nm sample this was 10.3 ± 2.6 nm, as shown in Figure 1. The red line is a Gaussian fit,

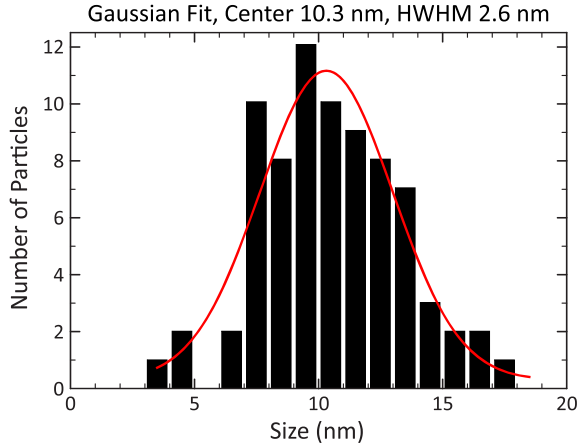

Figure 1. Gaussian fit (solid red line) to the distribution of sizes found from TEM micrographs from a sample set of 76 measurements for the nominal 10 nm size. The fitted maximum and HWHM is 10.3 ± 2.6 nm. A second analysis of a somewhat larger data set gave 9.6 ± 2.4 nm, for a weighted average of 10.0 ± 1.8 nm.

giving the HWHM value quoted above. A remeasurement of a larger data set gave 9.8 ± 2.4 nm, for a weighted average of 10.0 ± 1.8 nm. For the earlier-studied 7 nm size,[41] TEM measurements gave 7 ± 1.4 nm, while for the largest AuNP size of the present study this gave a mean value of 38 ± 8 nm.

From the BET analysis of N_2 adsorption, the bare SBA-15 samples had a typical surface area of ∼600 m^2/g, indicating a high porosity. For the AuNP-loaded SBA samples, the surface areas were similar though somewhat smaller at about 550 m^2/g on average, with a typical error of about 30 m^2/g. The average (adsorption/desorption) pore diameters for the pure silica were 7.6 nm, with errors expected to be in the 5% range. Smaller effective pore sizes were found for the AuNP samples, averaging to about 4.5 ± 0.3 nm, with a corresponding reduction in pore volume, averaging to 0.65 cm^3/g, within about 10%. This kind of "collapse" is well-known in the literature[49] and is also quite sample dependent.

It is noted, though the AuNP sizes and pore diameters were well established by the TEM and SEM analyses carried out, the sample morphologies and hence silica grain sizes and mesopore volumes are less well-known.[19,42−44,50,51] These could vary by a factor of 2 depending on the details of the synthesis procedure, which can influence the interpretation of the data discussed below. SEM imaging indicated silica grain sizes of order 1 μm but also showed that many grains were more spherical than the normal hexagonal shapes for mesoporous SBA-15 silica,[19] which could give a more random orientation of mesopores. For the AuNP samples, it is also important to note that the SBA-15 was templated in the presence of the nanoparticles,[42] with the silica then condensing around the liquid crystalline template, effectively trapping the stabilized AuNPs within the porous material; hence, their sizes are not restricted to that of the silica pores. Thus, in the extreme case here, the 38 nm AuNP can be stabilized even though the 7−8 nm pores of the silica host are much smaller.

3. μSR BASICS AND EXPERIMENTAL RESULTS

3.1. Muons and Sample Environment. Positive muons (μ^+) were produced at the TRIUMF accelerator near the University of British Columbia, with close to 100% spin polarization, such that in their decay ($\mu^+ \rightarrow e^+ + \nu_e + \overline{\nu}_\mu$), with a mean life of 2.2 μs, the e^+ is emitted preferentially *along* the muon spin, providing the essential feature of the μSR technique.[21,52,53] The amplitude of this asymmetric decay, appropriately known as the "asymmetry", has an intrinsic maximum value of 1/3, but is always empirically determined since it depends on a number of experimental factors. The present studies have been carried out with "surface muons", with an initial μ^+ kinetic energy of 4.1 MeV but which gets degraded to about 2 MeV in the sample cell, after passing through a beamline and target cell entrance window.[54]

The target cells and windows were made from nonmagnetic Ti metal and typically contained about 2 g of AuNP/silica powder in a sample volume of 5 mL (Table 1), though less for the 8 nm size, about 1.4 g, in a reduced sample volume of about 2.5 mL. The cells were made from two separate parts, an outer part to which the silica sample was added (and weighed) and an inner "plunger" part that compressed the sample to a higher density, more than sufficient to stop the μ^+ beam.

Loaded cells were placed in a magnetic spectrometer, with detection counters for both incident muons and decay positrons appropriately positioned, either in a longitudinal geometry (LF-μSR), parallel to the incident muon beam direction, or in a transverse geometry (TF-μSR), perpendicular to this direction. In TF-μSR, the muon spin precesses in the perpendicular plane and, because of the muon decay asymmetry, each time it sweeps past a positron counter array an enhanced decay probability is seen, giving rise to an oscillatory time dependence, as in Figures 2−5. In contrast, in LF-μSR, there is no precession and thus no oscillations in the measured asymmetry, as in Figures 6, 7, and 9.

To study the reaction rate of Mu with surface-adsorbed benzene (Bz), a known pressure of Bz vapor, measured with a capacitance manometer in a standard volume (SV) on the vacuum system (8.7 mL for the 8 nm, 10 nm AuNP and bare silica samples, 3 mL for the 38 nm AuNP), was let into a previously evacuated (to about 20 mTorr) sample cell. For an initial nominal monolayer loading on the AuNPs, upon first opening the Bz-loaded SV to the sample cell, the Bz pressure fell to near zero almost instantaneously, indicating rapid adsorption of Bz onto the AuNP surfaces, whereas it took noticeably longer for the bare silica,

The total number of AuNPs, N_{NP}, was estimated from the weight of added Au, assuming spherical NPs with the same density as bulk gold, giving (see Table 2 below) $N_{NP} \sim 1.2 \times 10^{16}$ for the 8 and 10 nm sizes and $\sim 1.3 \times 10^{14}$ for the 38 nm size. A similar estimate for the 7 nm AuNP studied earlier[41] gave $\sim 3 \times 10^{16}$ NPs. A nominal monolayer loading of Bz on the three AuNPs of the present study was estimated as follows. Since the AuNPs are located on the walls of the silica mesopores,[19] only half their surface area was assumed to be available for Bz adsorption. The surface area of an individual Bz molecule was found from its molecular geometry, assuming

DOI: 10.1021/acs.jpcc.9b08327
J. Phys. Chem. C 2019, 123, 27628−27642

Table 1. Measured Results for the Relaxation Rates, λ_{TF}, from the TF-μSR Data for the SBA-15 Silica and AuNP-Loaded Silica with and without Added Benzene, with [Bz] Determined by the Sample Cell Volume[a]

Sample	SV Pressure (Torr)[b]	μmol Bz[c]	[Bz][d]	Layers[e]	λ_{TF} (μs^{-1})
bare SBA-15 (0.45 g)[f]	0	–	–	–	0.22(2)
SBA-15 + Bz	7.5	3.5	4.2	–	0.27(2)
SBA-15 + Bz	30	14	16.8	–	0.85(6)
SBA-15 + Bz	60	28	33.7	–	1.4(1)
8 nm AuNP (1.4 g)[f]	0	–	–	–	3.8(3)
8 nm AuNP + Bz	7.6	3.5	8.4	0.7	4.1(3)
8 nm AuNP + Bz	15	7.0	16.6	1.4	5.7(5)
8 nm AuNP + Bz	30	14	33.5	2.8	6.3(5)
10 nm AuNP (2.4 g)[f]	0	–	–	–	8.8(9)
10 nm AuNP + Bz	21.5	10	12.0	1.4	10.7(6)
10 nm AuNP + Bz	83	38.5	46.3	5.3	14.5(15)
10 nm AuNP + Bz	115	53.5	64.2	7.5	15.2(28)
10 nm AuNP + Bz	208	96	115	13	23.6(38)
38 nm AuNP (2.8 g)[f]	0	–	–	–	6.7(6)
38 nm AuNP + Bz	12	1.9	2.3	1.6	6.5(7)
38 nm AuNP + Bz	48	7.7	9.2	6.3	8.8(10)
38 nm AuNP + Bz	98	15.6	18.8	13	8.7(10)
38 nm AuNP + Bz	198	31.7	38.0	26	12.3(15)

[a]Data taken at or near 300 K. [b]Measured Bz SV pressure (in Torr). Standard volumes are 8.7 mL for the 8 nm, 10 nm AuNP, and bare silica samples, 3 mL for the 38 nm NP. [c]The number of micromoles of Bz expected in each sample, from the measured SV pressures in (*b*), assuming an ideal gas. [d]Results from (*c*) converted to Bz concentration in the sample cell (5 mL for 10 nm, 38 nm, bare silica, but 2.5 mL for the 8 nm), in 10^{17} molecules/(cm^3). [e]Estimates of the number of flat Bz layers that could be formed on the AuNPs, determined from the effective surface area of an adsorbed Bz molecule discussed earlier. [f]Measured weight of each sample in the target cell, at 4.5 wt % Au for the 8 and 10 nm sizes but 2.5 wt % for the 38 nm size.

a perfect hexagon of area $A = 3/2\sqrt{3}l^2$, where l = 2.5 Å, the sum of the C−C and C−H bond lengths, giving A = 16.2 Å^2. However, to better ensure isolated benzenes on the AuNP surface, an extra 1 Å radius between adjacent benzenes was asssumed, giving then an effective surface area of 31.5 Å^2. The number of Bz molecules to cover all available AuNPs with a monolayer was then calculated as half of the AuNP area divided by this effective surface area of a Bz molecule. The pressure in the SV varied then from around 10−20 Torr for a nominal monolayer up to about 200 Torr at maximum multilayer loadings, depending on AuNP size, as given in Table 1.

3.2. Relaxation Rates in TF-μSR Studies.

In μSR studies in a TF, the total measured "asymmetry" at observation times, $A(t)$, has the form[38,52,53]

$$A(t) = \sum_i A_i e^{-\lambda_i t} \cos(\omega_i t + \phi_i) \quad (1)$$

where the index i labels different possible environments that the muon can be found in, formed on the time scale of the μ^+ slowing-down process, expected to be ∼10 ps in these powder samples, compared to measured values in the gas phase.[54] The parameters A_i, λ_i, ω_i and ϕ_i are respectively the initial asymmetry, the relaxation rate $(1/T_{2,i})$, the spin precession frequency ($\omega_i = 2\pi\nu_i$, where $\nu_i = \gamma_i B$, with γ_i the gyromagnetic ratio, and B the magnetic field strength), and the initial phase of the spin polarization of muons in their ith environment. In the present experiments, there are only two significant muon environments: diamagnetic or as the paramagnetic Mu atom (μ^+e^-). Thus, in a weak ($\lesssim$10 G) TF, the μSR signal $A(t)$ has the form

$$A(t) = A_{Mu} e^{-\lambda_{Mu} t} \cos(\omega_{Mu} t + \phi_{Mu}) + A_D e^{-\lambda_D t} \cos(\omega_D t + \phi_D) \quad (2)$$

where A_{Mu} is the amplitude of the Mu signal and A_D is that for diamagnetic muons. As seen in Figures 2−5, these signals are dominated by the precession of "triplet" S = 1 muonium,[54−56] due to the first term in eq 2. It is the Mu spin relaxation rates, $\lambda_{Mu} = \lambda_{TF}$ below, that are of prime interest here, though. All data were taken at or near 300 K.

Figure 2A shows the μSR signal for a sample of pure SBA-15 silica that had been heated at ∼150 °C and pumped overnight to remove O_2, compared with Figure 2B for a loading of 30 Torr Bz in the same sample. In contrast, for an unbaked/

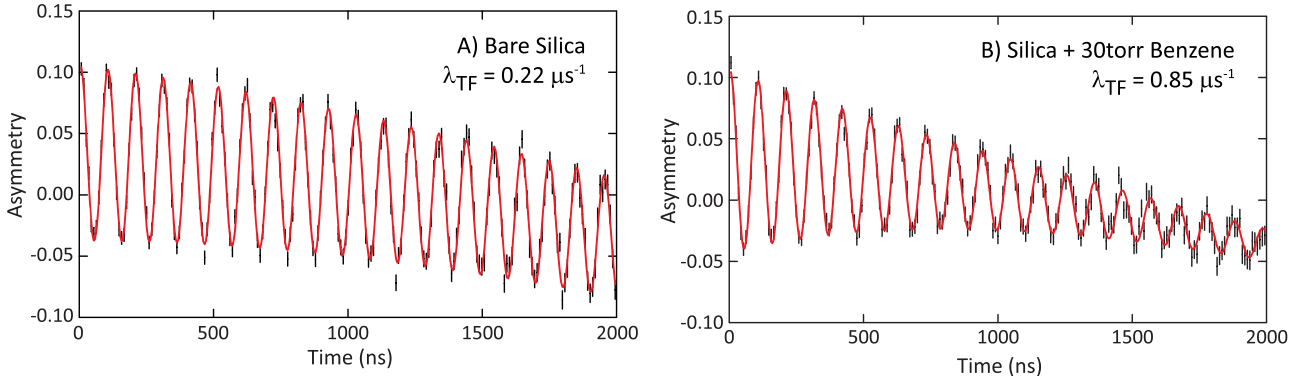

Figure 2. Mu precession in a ∼ 6 G TF at 300 K in pure SBA-15 silica (A), compared with that for a loading of 30 Torr Bz in the same silica (B). Solid lines are fits of eq 2 to the data for $A(t)$. In such a weak TF, diamagnetic muon precession appears as a time-dependent background.

DOI: 10.1021/acs.jpcc.9b08327
J. Phys. Chem. C 2019, 123, 27628−27642

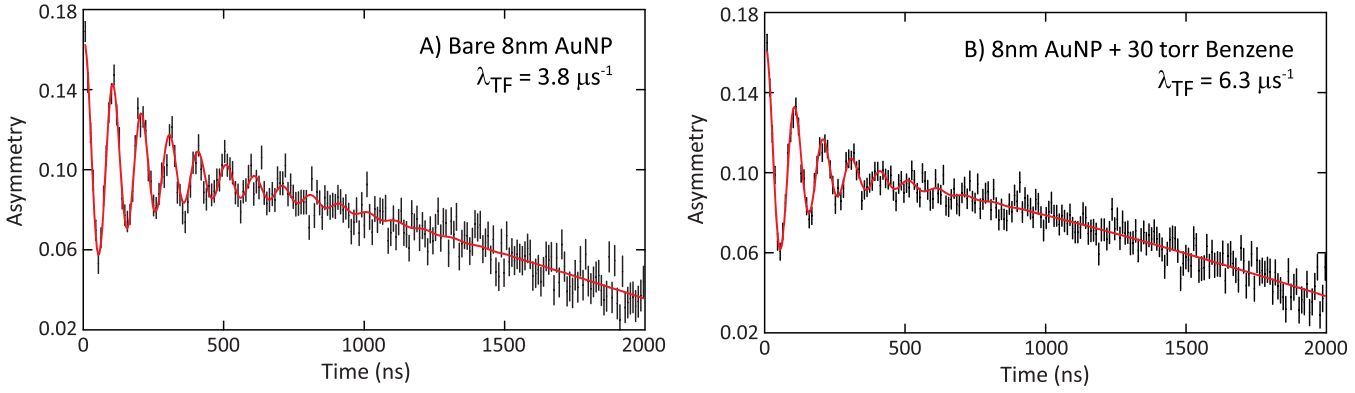

Figure 3. Mu precession in ~6 G TF at 300 K for the bare 8 nm AuNP/silica sample in A compared with a loading of 30 Torr Bz in the same sample in B, the same loading as in Figure 2B, here about 2 monolayers of Bz on this 8 nm AuNP surface. Solid lines are again fits of eq 2 to the data.

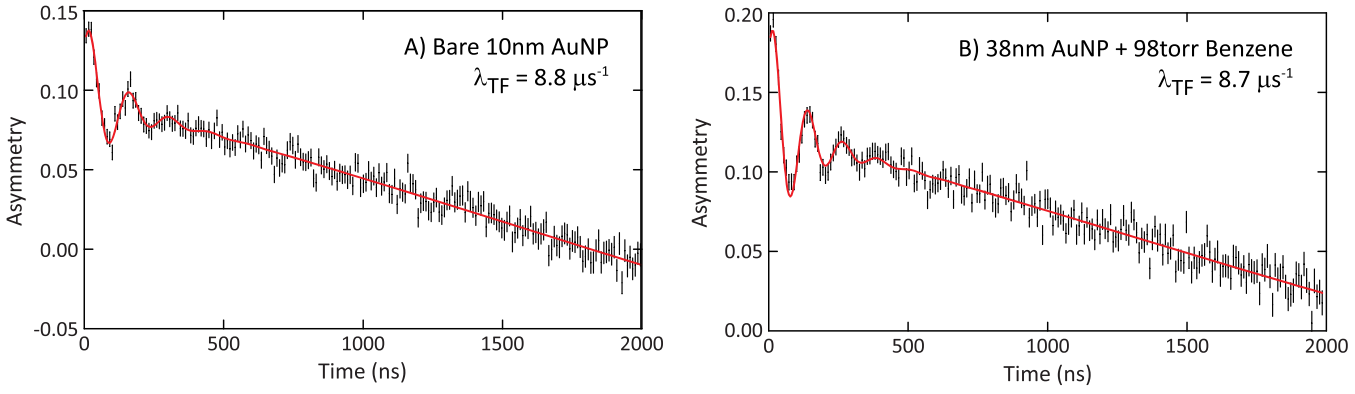

Figure 4. Mu precession signals in a ~6 G TF at 300 K for the bare 10 nm AuNP/silica sample in A compared with that for a loading of 21.5 Torr Bz in the same sample in B, corresponding to a monolayer of Bz on this AuNP. Solid lines are fits of eq 2 to the data. The faster relaxation rates seen in both A and B, compared to those in Figure 3 for the 8 nm AuNP, are due to a contribution from electron SE here.

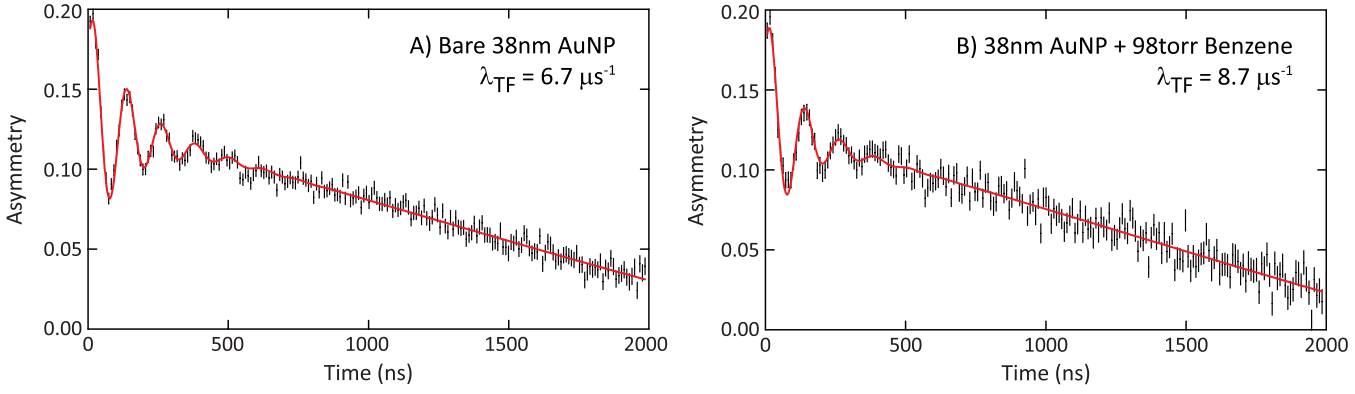

Figure 5. Mu precession signals in a ~6 G TF at 300 K for the bare 38 nm AuNP/silica sample in A compared with that for a loading of 98 Torr Bz in the same sample in B, corresponding to about 5 monolayers of Bz on this AuNP. See caption to Figure 4.

unpumped sample, essentially *no* Mu signal was seen at all,[42] suggesting that the large signals in Figure 2 are due to Mu located primarily in the silica mesopores, where any residual O_2, possibly occluded in water from the synthesis, would likely also be located, causing the loss of signal in the unbaked/unpumped samples.

The relaxation rate for the bare silica in Figure 2A, λ_{TF} = 0.22 ± 0.02 μs^{-1}, is contrasted with 0.85 ± 0.06 μs^{-1} for the 30 Torr Bz-loaded sample in Figure 2B, as recorded in Table 1. The slow Mu relaxation rate seen in Figure 2A could be due to a slight field inhomogeneity ($dB/B \sim 0.02$), which dephases the muon precession, or to paramagnetic impurities such as "dangling bonds" on the silica surface or to small amounts of residual O_2 from differences in heating/pumping times, with either/both of these causing spin relaxation of Mu due to electron spin exchange (SE) processes.[56,57] For the 30 Torr Bz-loaded sample in Figure 2B though, these factors would be the same, so the 4-fold faster relaxation rate seen demonstrates that Mu is reacting with the benzene, expected to be located in the silica pores,[17] as is the case for radical adsorbates bound to oxygen lattice sites in perovskites,[58] and here forming the MuC_6H_6 radical by the Mu + C_6H_6 addition reaction.[42] The

DOI: 10.1021/acs.jpcc.9b08327
J. Phys. Chem. C 2019, 123, 27628−27642

increased relaxation rate in the presence of Bz in Figure 2B is due to a plethora of μ-e-p eigenstates in the muoniated radical formed in a weak TF,[35,37,53,59] none of which are coherent with the frequency of the initial precessing Mu atom, thus causing a rapid dephasing of the muon spin.

Additional comparisons are shown in Figure 3 for a bare 8 nm AuNP in A compared with a loading of 30 Torr of Bz in B, the same as in Figure 2B for the pure silica, corresponding to about 2 monolayers on this AuNP surface; and in Figure 4 for a bare 10 nm AuNP in A compared with that for a loading of 21.5 Torr Bz in B, a nominal monolayer on this AuNP; followed by Figure 5 for a bare 38 nm AuNP in A compared with a loading of 98 Torr Bz in B, about 5 monolayers, all based on the estimate of effective benzene surface area given earlier. In all of these cases, noticeably faster relaxation rates are seen in the presence of the AuNPs compared to the bare silica, which establishes that Mu spends an appreciable fraction of its lifetime in a mesopore, where the AuNPs are located.[19] These rates are also faster again in the presence of added Bz as recorded in Table 1, along with other results for different Bz loadings on all three AuNP sizes of the present study. The relaxation rate, λ_{TF}, for the bare 8 nm AuNP in Figure 3A is interpreted as measuring the rate for Mu to diffuse to a AuNP located in a mesopore channel, where it reacts to form an adsorbed diamagnetic final state in the Mu + AuNP → MuAuNP reaction, with relaxation rate λ_C given in reaction scheme (R2) below.

Similar relaxation rates as seen in Figure 3A for the bare 8 nm AuNP were expected for the TF results in Figures 4A and 5A for the bare 10 and 38 nm AuNPs, respectively. However, λ_{TF} values for these sizes were twice as fast as for the bare 8 nm NP (Table 1), despite the fact that the number of 38 nm AuNPs in particular is 2 orders of magnitude lower (Table 2). We conclude from this that the enhancement in λ_{TF} seen in Figures 4A and 5A is due to Mu also undergoing electron SE with paramagnetic impurities 'P' in the silica host, which depolarizes the muon spin, causing a loss in the observable amplitude, A_{Mu} (eq 2).[56,57] In principle, such a SE process could also occur with the conduction electrons on the AuNP surfaces, as suggested in ref 5 for the stable nitroxyl radical on AuNPs in solution, but, if so, this SE relaxation effect should also be seen for the 8 nm AuNP in the present study and for the 7 nm AuNP in ref 41, contrary to observation in both cases.

The source of these paramagnetic impurities is again likely dangling bonds in the silica from the synthesis,[42,47] which may be present in greater amounts in the AuNP/silica samples than in the bare silica, since the silica matrix has to accommodate the NPs and/or residual O_2 arising from differences in heating/pumping times. This SE contribution, along with the chemisorption of Mu on the bare AuNP surface (λ_C), gives two parallel reaction paths:

$$\mathrm{Mu}(\Uparrow\uparrow) + \mathrm{P}(\downarrow) \xrightarrow{\lambda_{SE}} \mathrm{Mu}(\Uparrow\downarrow) + \mathrm{P}(\uparrow)\ , \qquad \text{(R1)}$$

$$\mathrm{Mu}(\Uparrow\uparrow) + \mathrm{AuNP} \xrightarrow{\lambda_C} \mathrm{Mu}(\Uparrow)\mathrm{AuNP}\ , \qquad \text{(R2)}$$

where the double arrow indicates the polarized muon spin state and the final product in (R2) is diamagnetic. (With respect to (R2), it is noted that, for a reaction of Mu with the unpaired electron on a Au atom, the MuAu product would be diamagnetic, but for reaction with a AuNP this would depend on the number of electrons at the Fermi surface. If the MuAuNP complex has an even number of electrons it would also be diamagnetic, but for an odd number there could be a small hyperfine interaction, though likely too small to be seen by the present TF studies (though possibly by an RF-resonance technique[60]), thus also appearing diamagnetic. It is also remarked that there was no evidence seen for the formation of a paramagnetic state from the Mu + AuNP study for a 7 nm AuNP in ref 41.) If the reaction rate in (R2) is fast enough, the full muon polarization can be transferred to the AuNP surface, so that the μ^+ can be a sensitive spin probe of surface magnetism.[41] It is remarked that ongoing studies using an RF-μSR resonance technique[60] have confirmed a diamagnetic final state in (R2) for the Mu + AuNP reaction.

3.3. Relaxation Rates in LF-μSR Studies: Bare AuNPs.

In a LF there is no spin precession, so the equivalent expression to eq 1 for the muon asymmetry has the simpler form

$$A_{LF}(t) = \sum_i A_i e^{-\lambda_i t} \qquad (3)$$

where the $\sum_i$ again represents different possible components of the muon polarization, with $\lambda_i = 1/(T_{1,i})$ here for their spin relaxation rates. In contrast as well to a TF-μSR experiment, where a reaction forming a diamagnetic muon final state, as for relaxation rate λ_C in (R2) above, can cause a dephasing of the muon spin,[41,61,62] in a LF a diamagnetic state is unaffected by the field. What causes a measurable effect in a LF is any kind of a muon spin-flip, analogous to a $1/T_1$ process in NMR,[53] illustrated by the $\mathrm{Mu}(\Uparrow\uparrow) + \mathrm{P}(\downarrow)$ SE reaction in (R1), where the electron spin-flipped Mu state $|\Uparrow\downarrow\rangle$, being a superposition of eigenstates of the spin Hamiltonian, oscillates as $|\Uparrow\downarrow\rangle \leftrightarrow |\Downarrow\uparrow\rangle$ at the hyperfine frequency of 4463.3 MHz, depolarizing the muon on a time scale of order 0.2 ns.[56,57,63]

Though not causing LF relaxation per se, the reaction rate λ_C does remove Mu atoms from the ensemble, thus causing a loss of amplitude of the Mu signal, leading to an asymmetry function of the form[41,57]

$$A_{LF}(t) = A_\mu(0) + A_{Mu}(X)\left\{e^{-(\lambda_C+\lambda_{SE})t} + \frac{\lambda_C e^{-\lambda_S t}}{\lambda_C + \lambda_{SE} - \lambda_S}(1 - e^{-(\lambda_C+\lambda_{SE}-\lambda_S)t}\right\} \qquad (4)$$

where $A_\mu(0)$ is a prompt amplitude formed during the muon slowing-down process and $A_{Mu}(X)$ is the asymmetry of the Mu signal as a function of LF ($X = B/B_0$, where B_0 is the hyperfine field, 1585 G for Mu), with $\lambda_C + \lambda_{SE} = \lambda_F$ below, a "fast" relaxation rate that dominates $A_{LF}(t)$ at early times, and λ_S is a "slow" relaxation rate that accounts for the possible spin relaxation of the diamagnetic MuAuNP product formed in (R2). For cases where the diamagnetic final state does not relax,[45,61,62] $\lambda_S = 0$ and one gets the simpler expression

$$A_{LF}(t) = A_\mu(0) + A_{Mu}(X)\left\{\frac{\lambda_C}{\lambda_C + \lambda_{SE}} + \frac{\lambda_{SE}}{\lambda_C + \lambda_{SE}} e^{-(\lambda_C+\lambda_{SE})t}\right\} \qquad (5)$$

Figures 6 and 7 show fits of the LF data to eq 4 at different fields for the 10 and 38 nm AuNPs, showing that the fast relaxation rates λ_F decrease with increasing field, a well-known

DOI: 10.1021/acs.jpcc.9b08327
J. Phys. Chem. C 2019, 123, 27628−27642

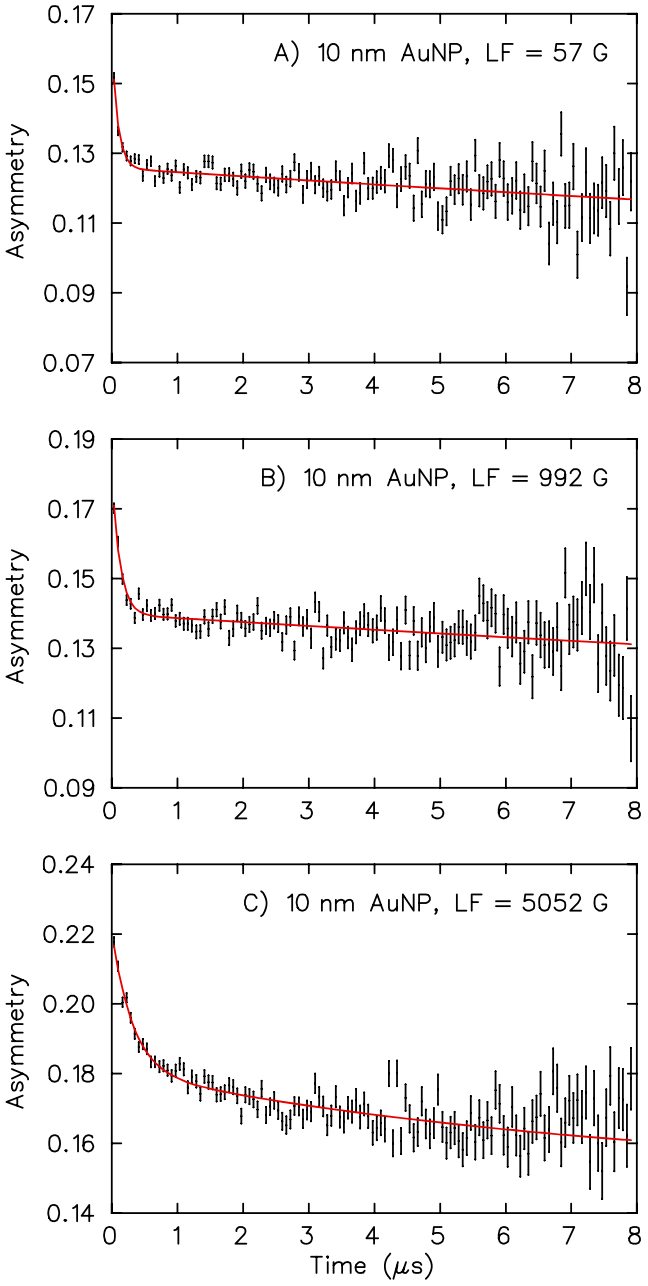

Figure 6. Representative asymmetry plots at different LFs for the bare 10 nm Au/SiO_2 sample, at 305 K. The solid lines are fits of the data to eq 4. Note the decreasing slope of the early time fast component with increasing LF.

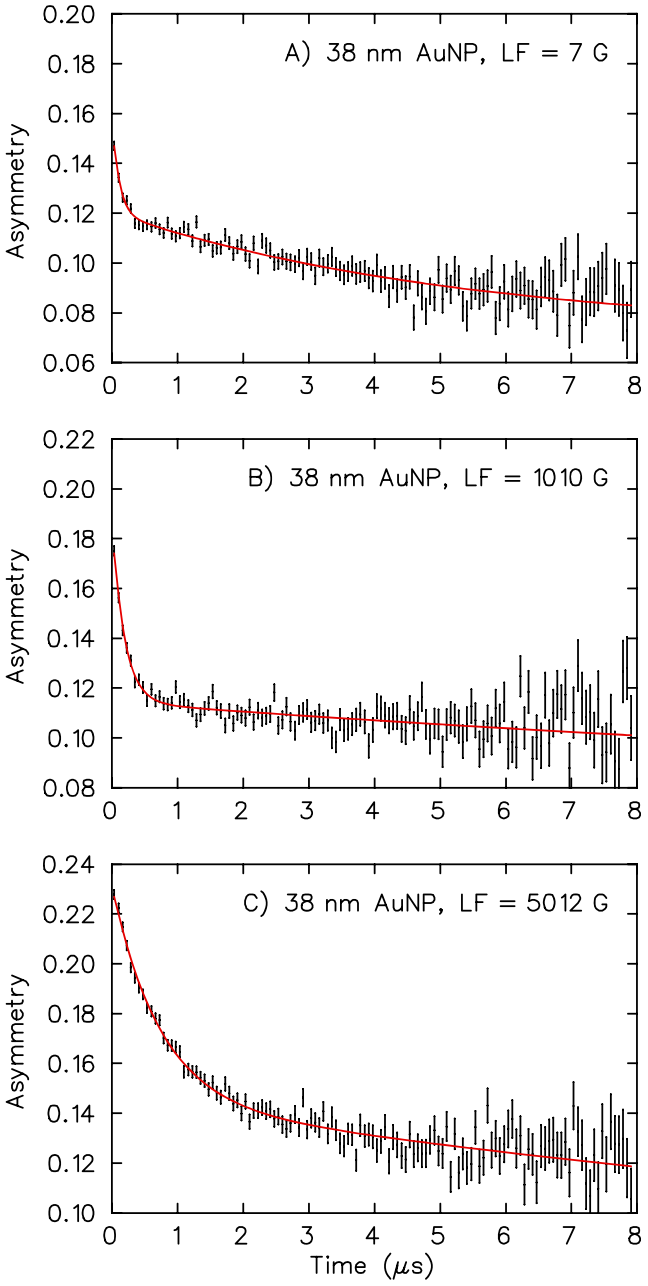

Figure 7. Representative LF asymmetry plots for the bare 38 nm AuNP/SiO_2 sample at 298 K. See caption to Figure 6. In both cases the amplitude of the "slow" component increases with field, most clearly seen from the nonrelaxing amplitude in eq 5.

signature of the quenching of SE relaxation of Mu by a LF, giving the result

$$\lambda_F = \lambda_C + \lambda_{SE} = \lambda_C + \lambda_{SE}^0 \times [1/(1 + X^2)] \quad (6)$$

where λ_{SE}^0 is the intrinsic electron SE rate seen at zero field. It is also noted that the amplitudes of the "slow" component in Figures 6 and 7 increase with field, seen most clearly from the nonrelaxing amplitude in eq 5, where $\lambda_{SE} \rightarrow 0$ as X becomes large ($B \gg B_0$ in eq 6) and since $A_{Mu}(X)$ also increases with increasing field.[61−63]

A plot of the results from fitting eq 6 to the measured fast relaxation rates λ_F for the bare 10 and 38 nm AuNP data, as seen in Figures 6 and 7, is shown in Figure 8. When X becomes large enough, SE is completely quenched (eq 6) and the intercepts in Figure 8 then give the reaction rates λ_C for the Mu + AuNP chemisorption reaction (R2); conversely, in weak fields, where $X \rightarrow 0$, $\lambda_F = \lambda_C + \lambda_{SE}^0$ is expected to be close to the value of λ_{TF} in the TF relaxation rates of Figures 4A and 5A.

The slopes and intercepts of the fitted lines in Figure 8 are as follows: $\lambda_{SE}^0 = 8.7 \pm 0.7\ \mu s^{-1}$ for the 10 nm AuNP sample (blue line) and $6.5 \pm 0.4\ \mu s^{-1}$ for the 38 nm AuNP sample (red line), with $\lambda_C = 1.9 \pm 0.2\ \mu s^{-1}$ and $0.55 \pm 0.16\ \mu s^{-1}$, respectively. For the 10 nm size, the sum $\lambda_{SE}^0 + \lambda_C = 10.6 \pm 0.8\ \mu s^{-1}$, somewhat larger than but close to $\lambda_{TF} = 8.8 \pm 0.9\ \mu s^{-1}$ (Figure 4A, Table 1), considering the errors; likewise for the 38 nm size where this sum is $7.1 \pm 0.4\ \mu s^{-1}$ compared with $\lambda_{TF} = 6.7 \pm 0.6\ \mu s^{-1}$ from the TF study (Figure 5A), both agreeing with expectation as commented above.

DOI: 10.1021/acs.jpcc.9b08327
J. Phys. Chem. C 2019, 123, 27628−27642

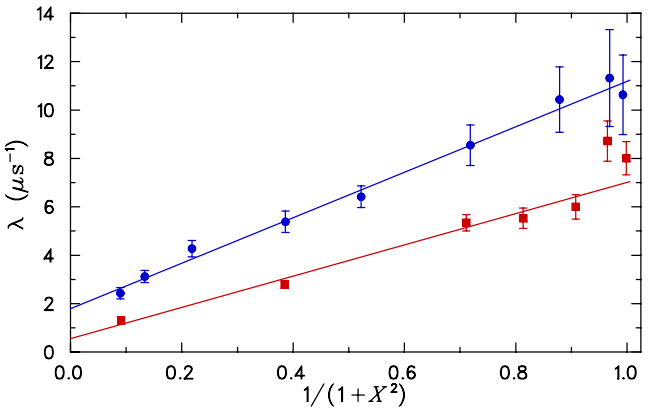

Figure 8. Plots of the "fast" LF relaxation rates, $\lambda_F = \lambda_C + \lambda_{SE}$, found from fits to the data as in Figures 6 and 7 for the bare AuNPs vs the SE "quenching" dependence defined by eq 6, for the 10 nm AuNP (blue circles and fitted line) and 38 nm AuNP (red squares and fitted line) . The slopes give the intrinsic SE relaxation rates, λ_{SE}^0, while the intercepts as $X \rightarrow \infty$ measure the slow chemisorption addition rates, λ_C.

In marked contrast to the LF data in Figures 6 and 7 though, for the 8 nm AuNP shown in Figure 9 there is essentially *no* fast relaxing component at all in a low LF of 200 G, demonstrating little or no SE contribution for this size, also the case in ref 41 for a 7 nm AuNP. Thus, the TF relaxation rate seen in Figure 3A, $\lambda_{TF} = 3.8 \pm 0.3\ \mu s^{-1}$ for the 8 nm size (Table 1), gives directly the value of λ_C for this smaller size. That SE is seen only for the 10 and 38 nm sizes (Figure 8) is almost surely due to differences in synthesis methods, affecting the sample morphology and hence the number of dangling bonds, or in sample preparation procedures, affecting the amount of residual oxygen.

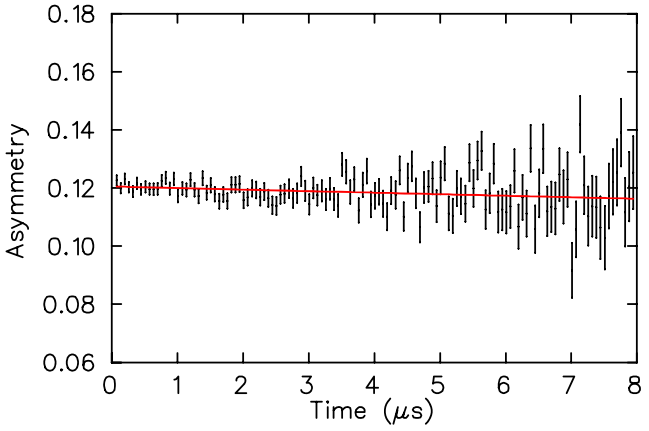

Figure 9. LF asymmetry plot for the bare 8 nm AuNP in a field of 200 G, showing essentially zero relaxation rate, indicating no SE contribution for this 8 nm AuNP, seen also in ref 41 for a 7 nm AuNP, both in contrast to the results in Figures 6 and 7. It is noted that the initial asymmetry is lower here than in these other LF figures due to difficulty in establishing the baseline for this very slowly relaxing 8 nm AuNP data.

4. MU SPIN RELAXATION RATES ON BARE AUNPS

The results described above, determining the relaxation rates λ_C for the chemisorption Mu + AuNP → λ_C MuAuNP reaction (R2), noting also that the high adsorption probability of atomic hydrogen on metal surfaces is well established,[64] are compared in Table 2 for the three AuNP sizes of the current study, along with the earlier result found for a 7 nm AuNP from ref 41. It is noted that the ratio of λ_C to the number of AuNPs, N_{NP} (column 3), is constant at about 2.5 to within 20% for the smallest particles, in accord with a previous remark that λ_C largely measures the inverse time taken for Mu to diffuse to a AuNP in a mesopore. Since λ_C can depend on grain size, it could in turn depend on differences in silica pore sizes, arising from the variability in sample morphology due to differences in synthesis procedures. However, the level of consistency noted above suggests that such effects are not playing as major a role here as might have otherwise been expected. (The 38 nm NP is not compared here since N_{NP} is 100 × smaller for this large size.) It is also noted that there can be considerable overlap in the smaller AuNP sizes, given the ∼20% spread seen in Figure 1, expected to be similar for all sizes.

A basis for interpreting the results in Table 2 for the relaxation rates λ_C on these different-sized AuNPs starts with a Langmuir model for surface-catalyzed reactions[65] of reactant 'A' interacting with surface 'S' to form products

$$A + S \rightleftharpoons A{\cdot}S \xrightarrow{k} \text{products} \qquad \text{(R3)}$$

where k is a (unimolecular) rate constant for the conversion of the adsorbed species to products, such that for a given surface coverage (θ) at low pressures,

$$-d[A]/dt = k\theta S_0 = kK_{Ads}S_0[A] \qquad (7)$$

with S_0 the total number of available sites (≫ than the total number of Mu atoms, monitored one at a time) and K_{Ads} is an equilibrium constant for the initial adsorption step shown in

Table 2. Results for the Reaction Rates λ_C at 300 K for the Mu + AuNP → MuAuNP Reaction for Different Sizes of AuNPs in the Pores of SBA-15 Silica

AuNP size (d, nm)[a]	λ_C (μs^{-1})[b]	N_{NP}[c]	ρ_{NP}(NPs cm^{-3})[d]	$\lambda_C/(\rho_{NP} \times \pi r^2 \times \bar{v})$[e]
7	8.4 ± 1.5[f,d]	2.9×10^{16}	5.8×10^{15}	$(5.0 \pm 1.2) \times 10^{-3}$
8	3.8 ± 0.3[g]	1.2×10^{16}	4.8×10^{15}	$(2.1 \pm 0.4) \times 10^{-3}$
10	1.9 ± 0.20[h]	1.1×10^{16}	2.2×10^{15}	$(1.5 \pm 0.3) \times 10^{-3}$
38	0.55 ± 0.16[h]	1.3×10^{14}	2.6×10^{13}	$(2.4 \pm 1.0) \times 10^{-3}$

[a]Nominal diameters of the AuNPs in this study, with a spread (HWHM) of about 20% for all sizes, as seen in Figure 1 for the 10 nm size. [b]Relaxation rates for the Mu + AuNP chemisorption reaction R2 with *bare* AuNP surfaces. Errors are statistical from the fits. [c]Estimated number of AuNPs in each sample, see earlier text. [d]The number density of AuNPs in the sample cell volume. [e]Ratio of λ_C to an assumed rate, given by $\rho_{NP} \times \pi r^2 \times \bar{v}$, with $\bar{v}$ the mean speed at 300 K. Errors broadened beyond statistical to account for some systematic error. [f]Obtained from refitting the TF data of ref 41 for a 7 nm AuNP to eq 2 herein the same function as used to fit the 8 nm AuNP data in this table. [g]Found directly from the TF results since there is no SE contribution here. [h]Found from the LF intercepts in Figure 8.

DOI: 10.1021/acs.jpcc.9b08327
J. Phys. Chem. C 2019, 123, 27628−27642

(R3),[65] with [A] being the pressure/concentration of reactant A. In the present context for product formation from (R3), where 'S' is the AuNP surface, forming a diamagnetic MuAuNP final state in a direct reaction step from (R2), wherein any intermediate [MuAuNP*] state that could form (see R4 below) is assumed to be essentially instantaneously stabilized due to its interactions with the AuNP surface on a time scale much faster than its dissociation lifetime. Thus, we can write the reaction rate from (R2,R3), in analogy with eq 7, as

$$-\mathrm{d}[\mathrm{Mu}]/\mathrm{d}t = \lambda_C[\mathrm{Mu}] = k_C \times \rho_{NP}[\mathrm{Mu}] \quad (8)$$

where $-\mathrm{d}[\mathrm{Mu}]/\mathrm{d}t$ signifies the rate loss of the "concentration" of a macroscopic ensemble of Mu atoms[57,59] interacting with the AuNP surface with rate constant k_C and ρ_{NP} is the number density of AuNPs in the sample volume (column 4, Table 2), effectively corresponding to (dimensionless) S_0 in eq 7. Since there is only one Mu atom in the system at a time,[34,53] ρ_{NP} stays constant during the reaction, giving the pseudo first-order kinetics result[65] defined by λ_C in eq 8.

Assuming a classical relaxation rate of Mu interacting with the AuNP (or SiO_2) surface of the form $\sim \sigma_C \times \rho_{NP} \times \bar{v}$, where $\bar{v}$ is the mean thermal velocity of Mu in the mesopores (7.5×10^5 cm s^{-1} at 300 K) and σ_C is the cross section for reaction, the values of λ_C in Table 2, normalized by this rate, should be constant in the *absence* of any specific size-dependent enhancement on the reaction rate of Mu with the AuNPs. These ratios are given in the last column of Table 2, where σ_C is assumed to be geometrical, πr^2 for the AuNP size. The factor of 2.5 increase seen for the 7 nm AuNP, compared to the average of the three larger AuNP sizes, suggests a catalytic enhancement for this smallest size.

However, since these samples were prepared at different times, this enhancement effect might also reflect a systematic difference in sample morphologies from differences in synthesis methodologies. There could also be some size overlap for the smaller AuNPs, given the ~20% spread seen in Figure 1 for the 10 nm size. It would have been important to follow this trend in λ_C for Mu reactivity on the bare AuNPs down to smaller AuNP sizes, well below 7 nm, where much larger changes in the normalized ratios in Table 2 could be expected, but it proved too difficult to reliably synthesize such samples for *un*capped AuNPs in SBA-15 silica by the methods used here. (New studies will focus on bare uncapped PtNPs, which can be made down to sizes even below 2 nm in SBA-15 silica.[19,66])

There is a further aspect of interest here though. From the previous claim that the relaxation rates λ_C (Table 2) largely determine the inverse time taken for Mu to diffuse to a AuNP in a silica mesopore, these times can be utilized to estimate an effective diffusion coefficient for muonium in the silica pores. Though Mu is expected to spend an appreciable fraction of its lifetime in the intergranular voids prior to re-entering a mesopore,[41,45] given that there are some 10^5 times more mesopores than grains or voids (argued below), it will also spend considerable time in a mesopore, where the AuNPs are located. (Interestingly, ref 67 reports on the smallest atom as a probe characterizing nanostructures, which would be the isotopic H atom, muonium, interacting with AuNPs explored herein.)

As a rough approximation, we adopt the classical result for homogeneous 1D diffusion,[33]

$$\langle x^2 \rangle = 2D_{Mu}t \quad (9)$$

where $\langle x^2 \rangle$ is the mean square displacement in time t between collisions of Mu with a AuNP in a silica mesopore. Given the typical SEM-determined pore length stated earlier of 1000 nm for a silica grain, the average number of AuNPs/mesopore is estimated to be ~0.1, which follows from knowing the BET-measured pore volumes for each sample (~0.65 cm^3/g) and the total number of AuNPs, N_{NP} in Table 2, giving $\langle x^2 \rangle^{1/2} \approx 1 \times 10^4$ nm/NP for the rms displacement in eq 9. Thus, from the inverse of λ_C in Table 2, for say the 10 nm size, t is $\sim 5 \times 10^{-7}$ s, giving $D_{Mu} \sim 1 \times 10^{-4}$ m^2 s^{-1} from eq 9. The values of D_{Mu} for all of the small AuNPs were found in the same way, giving an average value consistent with that for the 10 nm size above to within a factor of 2. (The 38 nm AuNP is much larger than the pore size, section 2.2, so it is much less likely to even be approximated as a 1D diffusion process.) Since there is some uncertainty in the number of NPs/mesopore, as well as an unknown fraction of time that Mu spends in a mesopore, along with the underlying assumption of homogeneous 1D diffusion, this value for D_{Mu} is just an order-of-magnitude estimate, at best, but even so it does provide a basis for comparison with Mu diffusion in other environments.

Thus, comparing with an early result for D_{Mu} in nonporous Cabosil silica grains ($\langle r^2 \rangle = 6Dt$ for 3D diffusion) of $\sim 2 \times 10^{-11}$ m^2 s^{-1} at 298 K,[68] gives a huge difference of 10^7 that reflects the vacuum-like nature of the mesopores, and which goes well beyond any effect that could arise from differences in sample morphology. Similarly so, in comparing with results for Mu diffusion in aqueous solutions,[69] giving $D_{Mu} \sim 1.3 \times 10^{-8}$ m^2 s^{-1} near 300 K, also orders of magnitude smaller than that estimated above for D_{Mu} in porous silica. Though D_{Mu} here is only a qualitative order-of-magnitude estimate, the value found of $\sim 10^{-4}$ m^2 s^{-1} is typical of what would be expected for the gaseous diffusion of such a light atom.[33,65] It is not known if D_{Mu} represents barrierless diffusion or not, but if not it is suggested that quantum diffusion of Mu in the silica mesopores may be playing a dominant role. It is remarked that nuclear quantum effects in the diffusion of H atoms on a PtO_2 surface have also been discussed recently.[70]

5. MU + BENZENE REACTION ON AUNP/SILICA SITES

5.1. Benzene Binding Sites and Energies. In a typical AuNP/silica sample weighing around 2 g (Table 1), there are about 10^{22} total SiO_2/SiOH sites. From the BET-determined pore volumes and the SEM-determined 1 μm grain size, there are $\sim 10^{17}$ mesopores distributed in 10^{13} silica grains, each mesopore with about 10^5 SiO_2 sites. It follows that the total surface area of the mesopores is some 100 times larger than for the exterior surfaces of the silica grains, so it is most likely that the added benzene resides *in* the pores, where the AuNPs are also located.[19] In contrast, as estimated above, there are only ~0.1 AuNPs per mesopore, qualitatively in accord with the measured TEM images and some 6 orders of magnitude less than the number of SiO_2/SiOH sites.

While it might then seem much more likely for benzene to be adsorbed at these many silica sites, differences in binding energy (BE) for adsorption/desorption will also be important. The probability for adsorption in the initial step of (R3) above (or R5 below) can be expected to scale as

$$P_{Ads} \propto N_{Sites} \times e^{-BE/(k_B T)} \quad (10)$$

DOI: 10.1021/acs.jpcc.9b08327
J. Phys. Chem. C 2019, 123, 27628−27642

in the absence of any activation-energy barrier,[65] where N_{Sites} are the number of available sites.

Gold metal has generally been considered quite inert, the noblest of all the metals,[71] though it is also now well established as being catalytically active for certain classes of reactions.[15] As would be expected, chemisorptive-like interactions of benzene on gold have higher BEs than for physisorption, seen in general for benzene on the coinage metals Cu(111), Ag(111), and Au(111), all giving BEs about 65 kJ/mol,[72] compared to physisorptive-like interactions of about 10 kJ/mol,[73,74] similar to that for the BE of benzene on bare silica surfaces.[75] We are unaware of any results for the BEs of benzene on AuNPs (expected to be much more catalytically active[1−5] than the bulk metal) or for benzene bound at SiO_2/SiOH sites in these silica environments. Assuming the same BEs on AuNPs as given above for benzene on gold metal, P_{Ads} at 300 K from eq 10 could be 3 orders of magnitude higher for benzene on AuNPs compared to neighboring silica sites, even with the much higher number of the latter.

It follows then, for nominal *monolayer* loadings, that benzene will be preferentially chemisorbed *on* the AuNPs in the mesopores of the AuNP/silica samples, in sync with an earlier remark that benzene vapor from the SV was adsorbed almost instantaneously for initial monolayer loadings. That benzene is located on the AuNPs would also be consistent with earlier muon level crossing resonance (LCR) studies,[42] where measurements of the temperature dependence of the strong Δ_1 signal amplitudes seen at similar loadings for the MuC_6H_6 radical on a 30 nm AuNP, arising from hyperfine anisotropy on the surface, showed that these signals were still clearly visible at temperatures near 420 K, whereas they were lost in the baseline on the bare silica by ∼350 K due to desorption and isotropic reorientation in the vapor phase. It can also be noted that the very observation of these LCR signals is good evidence that the added benzene reaches the AuNPs. Similar results were found in the present study at 300 K, to be reported separately.

5.2. Results for Mu + Bz on AuNP and Bare Silica Surfaces. H atom addition reactions have played a central role in chemical reactivity, including for their isotopic Mu-atom analogs,[34,37,40] and notably here for the Mu + Bz reaction in the gas phase[40] in comparison with this same reaction on the bare silica and AuNP surfaces. In the gas phase, Mu addition proceeds via a Lindemann−Hinshelwood mechanism,[37,65] attaining the high-pressure limit at (N_2/Ar) moderator pressures of a few bar for polyatomics. For the Mu + Bz reaction on a surface S we can write this as

$$\mathrm{Mu} + \mathrm{C_6H_6} \underset{k_d(\epsilon^*)}{\overset{k_{Bz}}{\rightleftharpoons}} [\mathrm{MuC_6H_6^*}] \xrightarrow[S]{k_s} \mathrm{MuC_6H_6{\cdot}S} \qquad \text{(R4)}$$

where k_{Bz} and k_S are rate constants for addition and stabilization of an intermediate excited-state $[MuC_6H_6^*]$ complex due to its interactions with the surface, respectively, and $k_d(\epsilon^*)$ is an energy-dependent unimolecular dissociation rate constant.[37,65] As in (R2) for Mu reactivity with bare AuNPs, $[MuC_6H_6^*]$ formed in (R4) should be stabilized on the AuNP surface on a time scale much faster than its dissociation lifetime (equivalent to the high-pressure limit in the gas phase), with the reaction rate then given by the rate constant k_{Bz} in a direct reaction step, as for k_C in eq 8. This may be the case for $[MuC_6H_6^*]$ at silica sites too, though with fewer degrees of freedom on the silica surface and a weaker BE, Mu dissociation would be more likely.

The reaction scheme in (R4) can be interpreted as an Eley−Rideal process[65,76−78] on AuNP or SiO_2 surfaces, starting with a similar form to (R3) but for adsorbed benzene from the vapor phase,

$$\mathrm{Bz} + \mathrm{AuNP} \rightleftharpoons \mathrm{Bz{\cdot}AuNP}$$

$$\mathrm{Mu} + \mathrm{Bz{\cdot}AuNP} \xrightarrow{k'} \text{products} \qquad \text{(R5)}$$

The experiment follows the loss of amplitude of the precessing Mu atom with time due to (R5), as shown by eq 2. The products in (R5) are not identified, but these would be expected to depend on the BE of the benzene to the surface. If it were strongly bound, a stabilized, possibly diamagnetic MuBz·AuNP product (recall parenthetical statement under R2) could form; but, if weakly bound, MuBz + AuNP would be likely products, in which case the reaction rate, leading to the dephasing of the muon spin in the MuC_6H_6 radical, could very well be similar to that seen in the gas phase.[40]

At low benzene pressures (Table 1), as in eq 7 above, from (R5) we obtain the rate expression

$$-\mathrm{d[Mu]}/\mathrm{d}t = k'\theta_{Bz}S_0[\mathrm{Mu}] = k''[\mathrm{Mu}][\mathrm{Bz}] \qquad (11)$$

since θ_{Bz} is $\propto$ [Bz],[65] with k' and k'' overall constants. Equation 11 is then written as

$$-\mathrm{d[Mu]}/\mathrm{d}t = \lambda_{Bz}[\mathrm{Mu}] = k_{Bz}[\mathrm{Bz}][\mathrm{Mu}] \qquad (12)$$

in analogy with eq 8, where λ_{Bz} is the relaxation rate for Mu addition to benzene adsorbed at surface sites, which is then rewritten to include a background rate in the absence of benzene, λ_B, as

$$\lambda_{Tot} = \lambda_B + \lambda_{Bz} = \lambda_B + k_{Bz}[\mathrm{Bz}] \qquad (13)$$

Here λ_B is taken to be the same as λ_C for the bare AuNPs in Table 2 for the AuNP/silica samples but equals 0.22 μs^{-1} for the bare silica from Figure 2A (Table 1), and [Bz] is in cm^{-3}, given its initial adsorption from the vapor phase.

It is the *chemical* addition rates for the Mu + C_6H_6 reaction of (R4) at surface sites that are relevant here. In contrast to the Mu + AuNP reactions of (R2), LF-μSR data were not taken for the Mu + Bz reaction, so it is only the TF relaxation rates, λ_{TF} from Table 1, that provide the basis for analysis. These must then be corrected for contributions from SE for the 10 and 38 nm sizes, given by the slopes λ^0_{SE} from Figure 8 of 8.7 and 6.5 μs^{-1}, respectively, as plotted for λ_{Tot} in Figure 10 below.

The concentration of benzene from eq 13 plotted in this figure was initially determined from the benzene vapor pressure in the SV, let into the cell volume; thus, [Bz] = n_{Bz}/V_{Cell} in Table 1 (fourth column). Results for the AuNP/silica samples are shown by the three upper color-coded points and fitted straight lines in Figure 10; the bottom **cyan** points and fitted line are for Mu + Bz in bare silica. The slopes give the rate constants, k_{Bz}, for Mu addition to surface-adsorbed benzene, listed in Table 3, based on the Eley−Rideal mechanism of (R5) and assuming as well homogeneous kinetics on a smooth AuNP surface. While some effect of different sample morphologies on these rates cannot be discounted, this is not likely to be nearly as significant an effect as that directly affecting λ_C on the bare AuNPs (Table 2), since λ_{Bz} here has been determined on these *same* AuNPs.

Though the cell volumes are well-known, the benzene concentration is better determined by the "free volume" that excludes the silica grains,

DOI: 10.1021/acs.jpcc.9b08327
J. Phys. Chem. C 2019, 123, 27628−27642

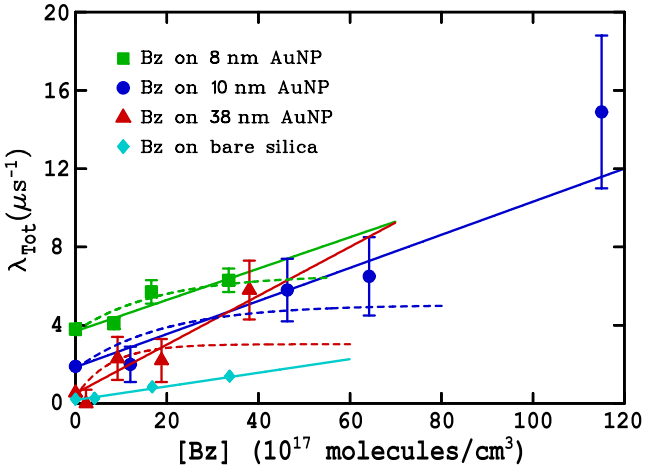

Figure 10. Chemical addition relaxation rates, λ_{Tot}, for Mu reactivity with benzene on the bare silica (lower cyan line) and AuNP samples (upper colored lines) vs [Bz] determined by V_{Cell}. The solid lines are fits of eq 13 to the data, giving rate constants, k_{Bz}, from the slopes. The error bars are statistical, smaller for the 8 nm AuNP size because there was no SE contribution in these data. The dashed lines show a possible asymptotic dependence from eq 15 for λ_{Tot} vs [Bz] for multiple benzene layers lying flat on the AuNP surfaces.

Table 3. Rate Constants (k_{Bz}) for the Mu + Bz → MuBz at 300 K to Surface-Adsorbed Bz in AuNP/Silica and Bare Silica Samples, Determined from the Linear Dependence Predicted by Eq 13, Assuming [Bz] Is Given by the Cell Volume (black entries) Compared with the Free Volume Results (blue entries)

Sample	$\lambda_B(\mu s^{-1})$[a]	k_{Bz} ($cm^3 s^{-1} \times 10^{-12}$)[b]
8 nm AuNP	3.8 ± 0.3	$(0.81 \pm 0.17) \times 10^{-12}$
8 nm AuNP	3.8 ± 0.3	$(0.62 \pm 0.13) \times 10^{-12}$
10 nm AuNP	1.9 ± 0.2	$(0.82 \pm 0.20) \times 10^{-12}$
10 nm AuNP	1.9 ± 0.2	$(0.69 \pm 0.16) \times 10^{-12}$
38 nm AuNP	0.55 ± 0.16	$(1.23 \pm 0.31) \times 10^{-12}$
38 nm AuNP	0.55 ± 0.16	$(0.95 \pm 0.24) \times 10^{-12}$
Bare Silica	0.22 ± 0.02	$(0.35 \pm 0.02) \times 10^{-12}$
Bare Silica	0.22 ± 0.02	$(0.33 \pm 0.02) \times 10^{-12}$

[a]Background relaxation rates, see eq 13. For the AuNPs λ_B is the same as λ_C for the bare AuNPs (Table 2), while for the bare silica this is the entry for λ_{TF} in Table 1 (from Figure 2A). [b]Rate constants, k_{Bz}, found from the slopes of the solid fitted lines to eq 13 in Figure 10, assuming [Bz] = n_{Bz}/V_{Cell} (black entries); and for [Bz] = n_{Bz}/V_{Free} (blue entries, not plotted), both from the Eley–Rideal mechanism of (R5). Errors are statistical only.

$$V_{Free} = V_{Cell} - V_{Grains} = V_{Cell} - M_{Pwd}/\rho_G \quad (14)$$

where V_{Cell} is 5 mL for the 10 nm, 38 nm AuNP, and bare silica samples but 2.5 mL for the 8 nm AuNP sample, M_{Pwd} is the mass of the silica powder in the sample cell (Table 1), and ρ_G is the density of silica. If we assume that ρ_G is given by the average density of 2.4 g/cm^3 betwen fused and polycrystalline quartz, then V_{Free} = 1.9, 4.0, and 3.8 cm^3 for the 8 nm, 10, and 38 nm AuNP samples, respectively. These smaller volumes compared to V_{Cell} give about a 25% increase in [Bz] compared to the entries in Table 1 (plotted in Figure 10), with a concomitant decrease in the values of k_{Bz} found from the slopes. The quartz reference here is nonporous so that V_{Free} = V_{Pores} + V_{Voids} for the silica mesopores and intergranular voids. The values of k_{Bz} found from these free-volume slopes (not plotted) are also given in Table 3, compared with the results determined by V_{Cell}, as in Figure 10. The dashed lines in this figure are explained below.

5.3. Discussion of These Mu + Bz Results. There are several important points that emerge from the linear plots in Figure 10 and the entries in Table 3. First, the values for k_{Bz} *are* different, between the 8 nm/10 nm samples, whose sizes can be expected to overlap, and the 38 nm AuNP samples, by a factor of 1.5 for both volume determinations and, more significantly, by a factor of 3 comparing the bare silica data in both data sets with the 38 nm AuNP size in Table 3 (2.5 on average for all sizes), demonstrating that the added benzene does *not* remain in the vapor phase in the mesopores (or in the intergranular voids) but is indeed surface-adsorbed.

Second, the linear fits from eq 13 are in good agreement with all the data (plotted only for [Bz] determined by the cell volume in Figure 10), in accord with the Eley–Rideal model of surface reactivity in (R5) above. Moreover, there is no indication of a change in slope, particularly for the 10 nm AuNP (blue points) up to the highest benzene concentrations, regardless of how [Bz] was determined, indicating a similar environment at all benzene loadings. It is also interesting that k_{Bz} tends to scale with AuNP size in Table 3, possibly reflecting the dependence on the number of available surface sites, S_0, in eq 11.

Third, the intercept (λ_B) for the bare silica data (cyan line in Figure 10) is much lower than for the AuNP/silica samples, given by λ_C for the bare AuNPs (Table 2), in accord with the claim above that the benzene in these samples is predominately *on* the AuNPs, as its higher BE for chemisorptive-like interactions would also lead us to expect.

Though the spread of 1.5 in the values of k_{Bz} between the 8/10 and 38 nm AuNP/silica samples in Table 3 is noteworthy, they do still overlap within error, giving an average value for Mu reactivity with surface-adsorbed benzene in these AuNP samples, from the free-volume values of [Bz] in Table 3, of $\langle k_{Bz} \rangle \sim (0.75 \pm 0.15) \times 10^{-12}$ cm^3 s^{-1}. That this average is enhanced by over a factor of 2 compared to the bare silica (and closer to 3 for the cell-volume values, where $\langle k_{Bz} \rangle \sim (0.95 \pm 0.20)$, same units) indicates a catalytic effect on the AuNPs due to the interaction of Mu with surface-adsorbed benzene on these NP surfaces.

There is a caveat here though. From the BET-determined pore diameters given earlier, the mesopore volumes for the AuNP/silica samples could be smaller than for the bare silica also by a factor of 2–3, *if* the silica grain sizes were the same, correspondingly increasing [Bz] in the mesopores and hence giving a value for k_{Bz} similar to the bare silica. On the other hand, given that there can be factor-of-two differences in grain sizes arising from uncertainties in the sample morphologies, the grain sizes here could just as well be different, in accord then with the 2–3-fold enhancement seen for the reaction of Mu with benzene on the AuNPs compared to the bare silica. It also seems physically reasonable that the Mu + Bz reaction rate on AuNPs (R5) would be faster than at silica sites, with the relatively larger BE for the chemisorption of benzene to AuNPs expected to give a more exoergic reaction and hence faster rates, particularly on early barrier potential energy surfaces.[34]

DOI: 10.1021/acs.jpcc.9b08327
J. Phys. Chem. C 2019, 123, 27628–27642

The measured rate constant for the Mu + Bz reaction in the gas phase, $k_{Bz}(gas) = (1.08 \pm 0.03) \times 10^{-12}$ cm^3 s^{-1} at 298 K,[40] is three times larger than on the bare silica in Table 3, which suggests a "steric effect"[65,79] reducing the cross section by this amount due to benzene being localized at SiOH sites in the silica environment, in contrast to its random motion in a gas. There could also be some effect here from Bz adsorption at silica sites. A similar steric effect would be expected for benzene at AuNP sites, in concert with the possible catalytic enhancement advanced above.

One would expect a minimum perturbation of the benzene ring bound to SiOH sites in bare silica compared to the gas phase, with a greater perturbation expected from the stronger BE to AuNPs. However, there is little or no evidence for any such perturbation on the NPs here, since the average rate constant from V_{Free} given above for these AuNP/silica samples, $\langle k_{Bz} \rangle = (0.75 \pm 0.15) \times 10^{-12}$ cm^3 s^{-1}, though somewhat lower than in the gas phase, almost overlaps with this value, reflecting the resonance stability of the benzene ring. This in turn echoes an earlier remark following (R5) that the BE of benzene chemisorbed to AuNPs is likely weaker than on bulk gold metal, giving rise then to a $Mu\dot{C}_6H_6$ product with an expected reaction rate similar to that seen in the gas phase.[40]

The time taken for Mu to find and react with a AuNP in a mesopore, diffusing between voids and mesopores in the process, should be similar for a bare AuNP and a Bz-covered one. (Differences in cross section will also play some role.) Given that the sizes of the AuNPs are all nominally larger than the mesopores (section 2.2), these NPs would be expected to block the mesopore channels. Hence, for a nominal monolayer loading, benzene lying flat on the AuNPs would give the largest cross section for Mu reactivity. Several studies in the literature have in fact shown that a monolayer of benzene does lie flat on a gold metal surface,[72−74,80,81] and that may be the case for the AuNPs here as well.

However, beyond a monolayer, were benzene to continue to lie flat on these AuNP surfaces, like stacked dinner plates, there would be no difference in the relaxation rates discussed earlier due to muon dephasing in the $Mu\dot{C}_6H_6$ radical formed, with each layer behaving in like manner to the one preceding it. This would then lead to an asymptotic dependence at higher loadings with zero slope, as shown by the dashed lines in Figure 10 for a simple phenomenological model of the form

$$\lambda_{Tot} = \lambda_C + N[Bz]/(C + D[Bz]) \quad (15)$$

for benzene concentrations $\lesssim 70 \times 10^{17}$ molecules/cm^3. The parameter 'N' fits to values in the range ∼0.44 to 0.28 from the 8 to 38 nm sizes, with 'C' ∼ 1.5 and 'D' fixed at values between 0.1 and 0.2. (There are too few data points to fit all parameters; the fit is also quite insensitive to D.)

Such an asymptotic-model dependence gives a qualitative account of the dependence of λ_{Tot} on [Bz] at these lower concentrations, albeit less so for the 38 nm AuNP, but this is clearly not the case for the 10 nm size up to its maximum value of $[Bz] = 115 \times 10^{17}$ molecules/cm^3. Though similar high loadings were not taken for the other NPs, there is no reason to expect that such a continued linear dependence would not be seen at higher loadings for these other sizes as well. We conclude then that there is *no* evidence for an asymptotic dependence, indicating multilayer Bz stacking on these AuNPs, with the linear fits shown in Figure 10 (and similarly so for the free-volume values of [Bz]) giving the best account of the data for the relaxation rates λ_{Tot} for the reactivity of Mu with surface-adsorbed benzene on the AuNPs in this study. That does raise a question though, how to account for this linear dependence?

The results of Lee et al. for benzene on a Cu(110) surface[82] are instructive in this regard. There it was shown that the second and subsequent layers of physisorbed benzene were canted on the first benzene layer, oriented essentially perpendicularly in "edge-on bonding", in analogy with the "T-shaped" geometry of the lowest energy states for the benzene dimer.[83,84] Could something similar be the case here for benzene adsorbed on the AuNPs?

If benzene were physisorbed on an initial chemisorbed benzene layer on these AuNPs, as in ref 82, we would expect to see a change in slope arising from the different BEs for these different environments, even at low loadings, as the asymptotic dependence shown by the dashed lines in Figure 10 indicates, and particularly so for the 10 nm AuNP up to its maximum loading. That this is not the case is in accord with earlier remarks that the Bz···AuNP interaction energies for monolayer loadings on the AuNPs are weaker than on gold metal[72,80] and perhaps even comparable to Bz···Bz physisorptive-like interactions.[73,74] If so, such synchronous interactions could give rise to similar orientation effects as described in ref 82 but canted over the whole range of benzene loadings on the AuNPs in the present study. It will take high-level quantum chemistry calculations to confirm though if this supposition is reasonable or not.

Still, there is already considerable evidence in the literature supporting this claim. In the calculations of Bilic et al.[73] for the physisorption of benzene on Cu surfaces, the geometric orientation of the benzene adsorbate had much more dramatic effects on the results than the small differences in binding energies seen due to these differences in orientation. Similarly as in the calculations of Granatier et al.,[74] where the adsorption of Bz to Au and Ag metal was found to be much weaker than its covalent interactions with Pd, dominated instead by dispersive forces with BEs of 4.2 and 2.3 kcals/mol, respectively, the value for gold perhaps in accord with the synchronous interactions suggested above. In unrestricted DFT calculations for small Pt and Pd metal clusters, tilted conformations due to enhanced interactions of benzene π bonds with the edges of these clusters were strongly favored.[85] Molecular orientation has also been discussed in hydrogen transfer reactions during free radical reactions in mesoporous silica.[16]

There is an alternate possibility here as well though to explain the linear dependence on [Bz] seen in Figure 10. Given that there is little likelihood of multiple benzenes at the many silica sites in these AuNP/silica samples, if individual benzenes were preferentially adsorbed at these silica sites at higher loadings, it could be that it is the reaction of Mu with benzene at these sites that is being observed.

While this possibility cannot be entirely ruled out, it also seems unlikely for a number of reasons. To begin with, recalling section 5.1, it would effectively mean equal BEs for Bz on AuNP and silica sites, contrary to literature expectations discussed above. Second, given this expected difference in BEs, a change in slope beyond monolayer loadings in the AuNP/silica samples would also be expected, similar to the slope seen in Figure 10 for the *bare* silica (cyan line), but this is also not observed. Finally, the aforementioned measurements of Level-Crossing Resonances,[42] at similar high Bz loadings as those in Figure 10, in both bare silica and AuNP/silica (and PtNP/

DOI: 10.1021/acs.jpcc.9b08327
J. Phys. Chem. C 2019, 123, 27628−27642

silica) samples, showed a clear difference in the *widths* of these signals near 300 K, about a factor of 2 narrower for the metal NP/silica samples, where the Bz is more strongly bound, which would not be the case if benzene were preferentially located at the silica sites.

6. CONCLUDING REMARKS

This paper describes a two-fold study of the reactivity of the isotopic hydrogen atom, muonium (Mu), with (i) *uncapped* bare AuNPs of different sizes, 8 nm, 10 nm, and 38 nm encapsulated in the heterogeneous environment of mesoporous SBA-15 silica, in comparison with an earlier study of 7 nm AuNPs in ref 41, and (ii) with benzene adsorbed at both bare silica sites and on the larger AuNPs in the silica mesopores.

In the case of the *bare* AuNPs, chemisorbed Mu on the AuNP surface forms a diamagnetic final state in the Mu + AuNP → MuAuNP reaction, described by a Langmuir-type reaction process on the AuNP surface. The measured relaxation rates for this reaction, λ_C, when normalized by a classical rate, appear to exhibit enhanced reactivity for a 7 nm AuNP by a factor of 2, though differences in sample morphology arising from the syntheses of these porous silica environments could also contribute to this difference.

Order-of-magnitude estimates of 1D diffusion coefficients were obtained from the λ_C relaxation rates, giving $D_{Mu} \sim 10^{-4}$ m^2 s^{-1}, several factors of ten faster than those found for Mu diffusion in other environments, suggest a possible role played by quantum diffusion of Mu in the silica mesopores.

In the second phase, the chemical addition rates of Mu with surface-adsorbed benzene (Bz) on the 8, 10, and 38 nm AuNPs in the AuNP/silica samples were studied over a range of Bz loadings, forming the muoniated cyclohexadienyl radical in the Mu + C_6H_6 → MuC_6H_6 addition reaction on the AuNP surfaces, compared with the same reaction in the gas phase and in bare SBA-15 silica.

An Eley−Rideal model of surface reaction rates predicts a linear dependence on total relaxation rate with Bz concentration, λ_{Tot}, for these Mu + Bz addition reactions in both the bare SBA-15 silica and the AuNP/silica samples (Figure 10), in good agreement with experiment. The resulting slopes give rate constants, k_{Bz}, that are 2−3 × faster on average than on the bare silica (Table 3), implying a catalytic enhancement in the Mu + C_6H_6 → MuC_6H_6 reaction due to the interaction of Mu with surface-adsorbed benzene on the AuNPs.

Even so, the average value $\langle k_{Bz} \rangle = (0.75 \pm 0.15) \times 10^{-12}$ cm^3 s^{-1}, found from the free-volume values of [Bz] for the Mu + Bz reactions on these AuNPs, is much the same as in the gas phase, indicating only a minor perturbation of the benzene ring due to its binding on AuNP surfaces. This in turn suggests that the BE of benzene to AuNPs may be considerably weaker than on bulk gold metal surfaces.

An alternate explanation for the trend in relaxation rates λ_{Tot} vs [Bz] was explored, which assumed multilayer benzenes lying flat on the AuNP surfaces at all benzene loadings. This leads to an asymptotic dependence with increasing [Bz], shown by the dashed lines in Figure 10, but which did not account for the data over the full range of benzene loadings nearly as well as the linear dependence predicted from the Eley−Rideal model.

Though it is possible that benzene could be located at the much more plentiful silica sites at the higher benzene loadings in the AuNP/silica samples, which could also give rise to a similar linear dependence on [Bz] as that seen in Figure 10, this seems unlikely for several reasons. In particular, were that the case, it would be expected to lead to a change in slope beyond monolayer loadings in Figure 10, contrary to observation.

These studies of the size dependence of the reaction rates of Mu both with uncapped bare AuNPs and with surface-adsorbed benzene on these NPs are, as far as we know, the only studies of their kind for any H atom in a heterogeneous mesoporous silica environment, and also represent then a "proof-of-principle" experiment. It is hoped that these studies will motivate quantum theory calculations of the reaction rates of H atoms with surface-adsorbed molecules on both gold and other metal NP surfaces, important systems in heterogeneous catalysis. Further studies of surface-adsorbed reactants by the μSR technique described herein on metal NPs, including PtNPs, which can be made down to sizes even below 2 nm in SBA-15 silica, along with measurements of their temperature dependences, are planned.

AUTHOR INFORMATION

Corresponding Author

*E-mail: flem@triumf.ca.

ORCID

D. G. Fleming: 0000-0002-6552-7044

M. J. MacLachlan: 0000-0002-3546-7132

Present Address

†(V.M.Z.) Instituto de Química, Universidade de São Paulo, cep 05508000, Brazil.

Notes

The authors declare no competing financial interest.

REFERENCES

(1) Daniel, M. C.; Astruc, D. Gold Nanoparticles: Assembly, Supramolecular Chemistry, Quantum-Size-Related Properties, and Applications toward Biology, Catalysis, and Nanotechnology. *Chem. Rev.* **2004**, *104*, 293−346.

(2) Alba-Molina, M.; Santiago, A. R. P.; Giner-Casares, J. J.; Martín-Romero, M. T.; Camacho, L.; Luque, R.; cano, M. Citrate-Stabilized Gold Nanoparticles as High-Performance Electrocatalysts: The Role of Size in the Electroreduction of Oxygen. *J. Phys. Chem. C* **2019**, *123*, 9807−9812.

(3) Yang, X.-F.; Wang, A.-Q.; Wang, W.-L.; Zhang, T.; Li, J. Unusual Selectivity of Gold Catalysts for Hydrogenation of 1,3-Butadiene toward cis-2-Butene: A Joint Experimental and Theoretical Investigation. *J. Phys. Chem. C* **2010**, *114*, 3131−3139.

(4) Laoufi, I.; Saint-Leger, M. C.; Lazzari, R.; Jupile, J.; Robach, O.; Garaudée, D. S.; Calbaith, G.; Dolle, P.; Crugel, H.; Bailly, A. Size and Catalytic Activity of Supported Gold Nanpoarticles:An in Operando Study during CO Oxidation. *J. Phys. Chem. C* **2011**, *115*, 4673−4679.

(5) Zhang, Z.; Berg, A.; Levanon, H.; Fessenden, R. W.; Meisel, D. On the Interaction of Free Radicals with Gold Nanoparticles. *J. Am. Chem. Soc.* **2003**, *125*, 7959−7963.

(6) Cuadrado, R.; Puetra, J. M.; Soria, F.; Cerda, J. I. A first principles study of thiol-capped Au nanoparticles: Structural, electronic, and magnetic properties as a function of thiol coverage. *J. Chem. Phys.* **2013**, *139*, 04319−1.

(7) Nealon, G. J.; Donnio, B.; Greget, R.; Kappler, J.-P.; Terazzi, E.; Gallani, J.-L. Magnetism in gold nanoparticles. *Nanoscale* **2012**, *4*, 5244−5258.

(8) Dehn, M. H.; Arseneau, D. J.; Buck, T.; Cortie, D. L.; Fleming, D. G.; MacFarlane, W. A.; King, S. R.; McDonagh, A. M.; McFadden, R. M. L.; Mitchell, D. R. G.; Kiefl, R. F. Nature of magnetism in thiol-capped gold nanoparticles investigated with Muon spin rotation. *Appl. Phys. Lett.* **2018**, *112*, 053105.

DOI: 10.1021/acs.jpcc.9b08327
J. Phys. Chem. C 2019, 123, 27628−27642

(9) Pensa, E.; Albrecht, T. Controlling the Dynamic Instability of Capped Metal Nanoparticles on Mertallic Surfaces. *J. Phys. Chem. Lett.* **2018**, *9*, 57−62.
(10) Alothman, Z. A. A Review: Fundamental Aspects of Silicate Mesoporous Materials. *Materials* **2012**, *5*, 2874−2902.
(11) Zhao, E. W.; Maligal-Ganesh, R.; Mentink-Vigier, F.; Zhao, T. Y.; Du, Y.; Oei, Y.; Huang, W.; Bowers, C. R. Atomic-Scale Structure of Mesoporous Silca-Encapsulated Pt and PtSn Nanoparticles Revealed by Dynamic Nuclear Polarization-Enhanced ^{29}Si MAS NMR Spectroscopy. *J. Phys. Chem. C* **2019**, *123*, 7299−7307.
(12) Chakraborty, D.; Chattaraj, P. K. Bonding, Reactivity, and Dynamics in Confined Systems. *J. Phys. Chem. A* **2019**, *123*, 4513−4531.
(13) Metiu, H. Preface to Special Topic: A Survey of Some New Developments in Heterogeneous Catalysis. *J. Chem. Phys.* **2008**, *128*, 182501-1−8.
(14) Gierada, M.; Profit, F. D.; Sulpizi, M.; Tielens, F. Understanding the Acidic Properties of the Amorphous Hydroxlated Silica Surface. *J. Phys. Chem. C* **2019**, *123*, 17343−17352.
(15) Vu, K. B.; Bach, L. G.; Tran, T. V.; Thuong, N. T.; Giang, H. N. Gold@silica catalyst: Porosity of silica shells switches catalytic reactions. *Chem. Phys. Lett.* **2019**, *728*, 80−86.
(16) Kidder, M. K.; Buchanan, A. C., III Effect of Pore Confinement and Molecular Orientation on Hydrogen Transfer During a Free-Radical Reaction in Mesoporous Silica. *J. Phys. Chem. C* **2008**, *112*, 3027−3031.
(17) Schwager, M.; Dilger, H.; Roduner, E.; Reid, I. D.; Percival, P. W.; Baiker, A. Surface difusion of the cyclohexadienyl radical adsdorbed on silica and on a silica-suppported Pd catalyst studied by means of ALC-μSR. *Chem. Phys.* **1994**, *189*, 697−712.
(18) Schwager, M.; Roduner, E.; Reid, I. D.; Kreitzman, S. R.; Percival, P. W.; Brodovitch, J.-C.; Leung, S.-K.; Sun-Mack, S. Surface Dynamics of the Cyclohexadienyl Radical Adsorbed on Silica Gel Investigated Using Avoided Level-Crossing Muon Spin Resonance. *Z. Phys. Chem.* **1995**, *190*, 29−40.
(19) Song, H.; Rioux, R. M.; Hoefelmeyer, J. D.; Komor, R.; Niesz, K.; Grass, M.; Yang, P.; Somorjai, G. A. Hydrothermal Growth of Mesoporous SBA-15 Silica in the Presence of PVP-Stabilized Pt Nanoparticles: Synthesis, Characterization and Catalytic Properties. *J. Am. Chem. Soc.* **2003**, *128*, 3027−3037.
(20) Xue, M.; Zink, J. I. Probing the Microenvironment in the Confined Pores of Mesoporous Silica Nanoparticles. *J. Phys. Chem. Lett.* **2014**, *5*, 839−842.
(21) Fleming, D. G.; Arseneau, D. J.; Shelley, M. Y.; Beck, B.; Dilger, H.; Roduner, E. μSR Studies of Hyperfine Couplings and Molecular Interactions of the Mu-Cyclohexadienyl Radical in Y-Zeolites and in Solid Bulk Benzene. *J. Phys. Chem. C* **2011**, *115*, 11177−11196.
(22) Rhodes, C. J.; Butcher, E. C.; Morri, H.; Reid, I. D. Mobility of Radicals in Zeolite Catalysts: Molecular Motion Studied by Muon Spectroscopy. *Magn. Reson. Chem.* **1995**, *33*, S134−S146.
(23) Haw, J. F. Zeolite acid strength and reaction mechanisms in catalysis. *Phys. Chem. Chem. Phys.* **2002**, *4*, 5431.
(24) Yun, J. H.; Lobo, R. F. Radical Cation Intermediates in Propane Dehydrogenation and Propene Hydrogenation over H-[Fe] Zeolites. *J. Phys. Chem. C* **2014**, *118*, 27292−27300.
(25) Zalazar, F. M.; Cabral, N. D.; Ojeda, G. D. R.; Alégra, C. I. A.; Peruchena, N. M. Confinement Effects in Protonation Reactions Catalyzed by Zeolites with Large Void Structures. *J. Phys. Chem. C* **2018**, *122*, 27350−27359.
(26) Hensen, E. M. J.; Poduval, D. G.; Ligthart, D. A. J. M.; van Veen, J. A. R.; Rigutto, M. S. Quantification of Brøsted Acid Sites in Aluminosilicates. *J. Phys. Chem. C* **2010**, *114*, 8363−8374.
(27) Venuto, P. B. *Stud. Surf. Sci. Catal.* 1997, *105*, 811.
(28) Werst, D. W.; Han, P.; Chousse, S. C.; Vinokur, E. I.; Xu, L.; Trifunic, A. D.; Erikson, L. A. Hydrogen Atom Addition to Hydrocarbon Guests in Radiolyzed Zeolites. *J. Phys. Chem. B* **1999**, *103*, 9219.
(29) Hama, T.; Ueta, H.; Kouchi, A.; Watanabe, N.; Tachikawa, H. Quantum Tunneling Hydrogenation of Solid Benzene and Its Control via Surface Structure. *J. Phys. Chem. Lett.* **2014**, *5*, 3843−3848.
(30) Carley, A. F.; Edwards, H. A.; Mile, B.; Wyn Roberts, M.; Rowlands, C. G.; Hancock, F. E.; Jackson, D. S. Applications of EPR to a study of the hydrogenation of ethene and benzene over a supported Pd catalyst: detection of free radicals on a catalyst surface. *J. Chem. Soc., Faraday Trans.* **1994**, *90*, 3341.
(31) Lutterloh, C.; Biener, J.; Schenck, A.; Küppers, J. Interaction of D(H) atoms with physisorbed benzene and (1,4)- dimethyl-cyclohexane: Hydrogenation and H abstraction. *J. Chem. Phys.* **1996**, *104*, 2392−2400.
(32) Huang, W.; Li, W.-X. Surface and interface design for heterogeneous catalysis. *Phys. Chem. Chem. Phys.* **2019**, *21*, 523−526.
(33) Roduner, E. *Nanoscopic Materials: Size-Dependent Phenomena and Growth Principles*, 2nd ed.; Royal Society of Chemistry, 2014.
(34) Baer, S.; Fleming, D. G.; Arseneau, D. J.; Senba, M.; Gonzalez, A. C. In *Kinetic isotope effects in gas-phase muonium reactions*; Kaye, J., Ed.; ACS Advances in Chemistry Symposium Series; 1992; No. *502*, pp 111−137.
(35) Roduner, E. Polarized positive muons probing free radicals: a variant of magnetic resonance. *Chem. Soc. Rev.* **1993**, *22*, 337.
(36) Fleming, D. G.; Manz, J.; Sato, K.; Takayanagi, T. Fundamental Change in the Nature of Chemical Bonding by Isotopic Substitution. *Angew. Chem., Int. Ed.* **2014**, *53*, 13706−13709.
(37) Arseneau, D. J.; Garner, D. M.; Reid, I. D.; Fleming, D. G. Muonium Addition Reactions and Kinetic Isotope Effects in the Gas Phase: k_∞ Rate Constants for Mu + C_2H_2. *J. Phys. Chem. A* **2015**, *119*, 7247−7256.
(38) Fleming, D. G.; Arseneau, D. J.; Sukhorukov, O.; Brewer, J. H.; Mielke, S. L.; Truhlar, D. G.; Schatz, G. C.; Garrett, B. C.; Petrson, K. A. Kinetics of the reaction of the heaviest hydrogen atom with H2, the 4He + H2 → 4HeH + H reaction: Experiments, accurarte quantal calculations, and variational transition state theory, including kinetic isotope effects for a factor of 36.1 in atomic mass. *J. Chem. Phys.* **2011**, *135*, 184310-1−18.
(39) Jambrina, P. G.; García, E.; Herrero, V. J.; Saéz-Rábanos, V.; Aoiz, F. J. Dynamics of the reactions of muonium and deuterium atoms with vibrationally excited hydrogen molecules: tunneling and vibrational adiabaticity. *Phys. Chem. Chem. Phys.* **2012**, *14*, 14596−14604.
(40) Roduner, E.; Louwrier, P. W. F.; Brinkman, G. A.; Garner, D. M.; Reid, I. D.; Arseneau, D. J.; Senba, M.; Fleming, D. G. Quantum Phenomena and Solvent Effects on Addition of Hydrogen Isotopes to Benzene and Dimethylbutadiene. *Ber. Bunsenges. Phys. Chem.* **1990**, *94*, 1224−1230.
(41) Dehn, D. H.; Arseneau, D. J.; Böni, P.; Bridges, M. D.; Buck, T.; Cortie, D. L.; Fleming, D. G.; Kelly, J. A.; MacFarlane, W. A.; MacLachlan, M. J.; McFadden, R. M. L.; Morris, G. D.; Wang, P. W.; Xiao, J.; Zamarion, V. M.; Kiefl, R. F. Communication: Chem-isorption of muonium on gold nanoparticles: A sensitive new probe of surface magnetism and reactivity. *J. Chem. Phys.* **2016**, *145*, 181102−5.
(42) Xiao, J.; Arseneau, D. J.; Bridges, M. D.; Cortie, D.; Cottrell, S. P.; Dehn, M.; Fleming, D. G.; Kelly, J.; Kiefl, R. F.; MacFarlane, W. A.; MacLachlan, M.; McKenzie, I. *Interaction of the Mu-cyclohexadienyl radical with metallic (Au, Pt) nanoparticles in mesoporous silica*; Journal of Physics: Conf. Series; 2014; *551*, pp012044-1−6; Xiao, J. M.Sc. Thesis, Dept. of Chemistry, University of British Columbia, 2014.
(43) Grasseschi, D.; Ando, R. A.; Toma, H. E.; Zamarion, V. M. Unraveling the nature of Turkevich gold nanoparticles; the unexpectyed role of the dicarboxyketone species. *RSC Adv.* **2015**, *5*, 5716−5724.
(44) Kruk, M.; Cao, L. Pore Size Tailoring in Large-Pore SBA-15 Silica Synthesized in the Presence of Hexane. *Langmuir* **2007**, *23*, 7247−7254.
(45) Dehn, M. H.; Arseneau, D. J.; Bridges, M. D.; Buck, T.; Cortie, D. L.; Cottrell, S. P.; Fleming, D. G.; Kelly, J. A.; MacFarlane, W. A.; MacLachlan, M. J.; Morris, G. D.; McKenize, I.; Xiao, J.; Kiefl, R. F.

DOI: 10.1021/acs.jpcc.9b08327
J. Phys. Chem. C 2019, 123, 27628−27642

Spin Depolarization of Muonium in Mesoporous Silica. *Journal of Physics: Conf. Series* **2014**, *551*, 012006-1−5.
(46) Dinkel, R.; Jakobi, J.; Ziefuss, A. R.; Barcikowski, S.; Braunschweig, B.; Peukert, W. Role of Citrate and NaBr at the Surface of Colloidal Gold Nanoparticles during Functionalization. *J. Phys. Chem. C* **2018**, *122*, 27383−27391.
(47) Inaki, Y.; Yoshida, H.; Yoshida, T.; Hattori, T. Active Sites on Mesoporous and Amorphous Silica Materials and Their Photocatalytic Activity: An Investigation by FTIR, ESR, VUV-UV and Phtoluminescence Spectroscopies. *J. Phys. Chem. B* **2002**, *106*, 9098−9106.
(48) Ojea-Jimenez, I.; Bastus, N. G.; Puntes, V. Influence of the Sequence of the Reagents Addition in the Citrate-Mediated Synthesis of Gold Nanoparticles. *J. Phys. Chem. C* **2011**, *115*, 15752−15757.
(49) Naik, B.; Hazra, S.; Prasad, V. S.; Ghosh, N. H. Synthesis of Ag nanoparticles within the pores of SBA-15: An efficient catalyst for reduction of 4-nitrophenol. *Catal. Commun.* **2011**, *12*, 1104−1108.
(50) Chiang, Y.-D.; Lian, H.-Y.; Leo, S.-Y.; Wang, S.-G.; Yamauchi, Y.; Wum, K. C-W. Controlling Particle Size and Structural Properties of Mesoporous Silica Nanoparticles Using the Taguchi Method. *J. Phys. Chem. C* **2011**, *115*, 13158−13165.
(51) Phan, H. T.; Haes, A. J. What Does Nanoparticle Stability Mean? *J. Phys. Chem. C* **2019**, *123*, 16495−16507.
(52) Yaouanc, A.; Delmas de Reotier, D. *Muon Spin Rotation, Relaxation and Resonance, Applications to Condensed Matter*; Oxford Univ. Press, 2011.
(53) Roduner, E. Muon Spin Resonance- A variant of magnetic resonance. *Appl. Magn. Reson.* **1997**, *13*, 1.
(54) Senba, M.; Arseneau, D. J.; Pan, J. J.; Fleming, D. G. Slowing-down times and stopping powers for ∼ 2- MeV μ^+ in low-pressure gases. *Phys. Rev. A: At., Mol., Opt. Phys.* **2006**, *74*, 042708−17.
(55) Johnson, C.; Cottrell, S. P.; Ghandi, K.; Fleming, D. G. Muon implantation in inert gases studied by radio frequency spectroscopy. *J. Phys. B: At., Mol. Opt. Phys.* **2005**, *38*, 119−134.
(56) Senba, M.; Fleming, D. G.; Arseneau, D. J.; Garner, D. M.; Reid, I. D. Muonium depolarization by electron spin exchange with O_2 gas in the temperature range 90−500 K. *Phys. Rev. A: At., Mol., Opt. Phys.* **1989**, *39*, 3871−3883.
(57) Turner, R. R.; Snider, R. F.; Fleming, D. G. Spin relaxation of hydrogen-atom isotopes via electron spin exchange with paramagnetic gases. *Phys. Rev. A: At., Mol., Opt. Phys.* **1990**, *41*, 1505−1516.
(58) Fung, V.; Wu, Z.; Jiang, De-en. New Bonding Model of Radical Adsorbate on Lattice Oxygen of Peroskovites. *J. Phys. Chem. Lett.* **2018**, *9*, 6321−6325.
(59) Duchovic, R. J.; Wagner, A. F.; Turner, R. E.; Garner, D. M.; Fleming, D. G. The analysis of muonium hyperfine interaction measurements of thermal rate constants for addition reactions. *J. Chem. Phys.* **1991**, *94*, 2794.
(60) Fleming, D. G.; Cottrell, S. P.; McKenzie, I.; Ghandi, K. G. Rate constants for the slow Mu + propane abstraction reaction at 300 K by diamagnetic RF resonance. *Phys. Chem. Chem. Phys.* **2015**, *17*, 19901−19910 (similar studies of bare AuNP surfaces are in progress).
.
(61) Pan, J. J.; Senba, M.; Arseneau, D. J.; Gonzalez, A. C.; Kempton, J. R.; Fleming, D. G. Mu + NO Kinetic Isotope Effects in Unimolecular Dissociation. *J. Phys. Chem.* **1995**, *99*, 17160−17168.
(62) Pan, J. J.; Senba, M.; Arseneau, D. J.; Fleming, D. G.; Himmer, U.; Suzuki, Y. Measurements of Mu + NO termolecular kinetics up to 520 bar: isotope effects and the Troe theory. *Phys. Chem. Chem. Phys.* **2000**, *2*, 621−631.
(63) Himmer, U.; Dilger, H.; Roduner, E.; Pan, J. J.; Arseneau, D. J.; Fleming, D. G.; Senba, M. Kinetic Isotope Effect in the gas phase reaction of Muonium with molecular oxygen. *J. Phys. Chem. A* **1999**, *103*, 2076−2087.
(64) Jiang, H.; Dorenkamp, Y.; Krüger, K.; Bünermann, O. Inelastic H and D atom scattering from Au(111) as benchmark for theory. *J. Chem. Phys.* **2019**, *150*, 184704.
(65) Steinfeld, J. I.; Fransico, J. S.; Hase, W. L. *Chemical Kinetics and Dynamics*, 2nd ed.; Prentice Hall, 1999.
(66) Li, J.; Zhang, Y.; Zheng, J. Intermolecular energy flows between surface molecules on metal nanoparticles. *Phys. Chem. Chem. Phys.* **2019**, *21*, 4240−4245.
(67) Hiratsuka, Y.; Tanaka, H.; Miyahara, T. What is the Smallest Atom as a Probe for Characterizing Nanostructures? *J. Phys. Chem. C* **2018**, *122*, 15446−15455.
(68) Marshall, G. M.; Warren, J. B.; Garner, D. M.; Clark, G. S.; Brewer, J. H.; Fleming, D. G. Production of Thermal Muonium in the Vacuum Between the Grains of Fine Silica Powders. *Phys. Lett. A* **1978**, *65*, 351−358.
(69) Walker, J. A.; Mezyk, S. P.; Roduner, E.; Bartels, D. M. Isotope Dependence and Quantum Effects on Atomic Hydrogen Diffusion in Liquid Water. *J. Phys. Chem. B* **2016**, *120*, 1771−17790.
(70) Yang, Y.; Kawazoe, Y. Adsorption and Diffusion of H Atoms on β-PtO_2 Surface: The Role of Nuclear Quantum Effects. *J. Phys. Chem. C* **2019**, *123*, 13804−13811.
(71) Hammer, B.; Nørskov, J. K. Why gold is the noblest of all the metals. *Nature* **1995**, *376*, 238−240.
(72) Liu, W.; Maass, F.; Willenockel, M.; C. Bronner, C.; Schulze, M.; Soubactch, S.; Tautz, F. S.; Tegender, P.; Tkatchenko, A. Quantitative Prediction of Molecular Adsorption: Structure and Binding of Benzene on Coinage Metals. *Phys. Rev. Lett.* **2015**, *115*, 036104-1−5.
(73) Bilic, A.; Reimers, J. R.; Hush, N. S.; Hoft, R. C.; Ford, M. J. The Adsorption of Benzene on Copper, Silver and Gold Surfaces. *J. Chem. Theory Comput.* **2006**, *2*, 1093−1105.
(74) Granatier, J.; Lazar, P.; Otyepka, M.; Hobza, P. The Nature of the Binding of Au, Ag and Pd to Benzene, Coronene, and Graphene: From Benchmark CCSD(T) Calculations to Plane-Wave DFT Calculations. *J. Chem. Theory Comput.* **2011**, *7*, 3743−3755.
(75) McKenzie, M. E.; Goyal, S.; Lee, S. H.; Park, H.-H.; Savoy, E.; Rammohan, A. R.; Mauro, J. C.; Kim, H.; Min, K.; Cho, E. Adhesion of Organic Molecules on Silica Surfaces: A Density Functional Theory Study. *J. Phys. Chem. C* **2017**, *121*, 392−401.
(76) Weinberg, W. H. Eley-Rideal Surface Chemistry: Direct Reactivity of Gas Phase Atomic Hydrogen with Adsorbed Species. *Acc. Chem. Res.* **1996**, *29*, 479−487.
(77) Chen, J.; Zhou, X.; Jiang, B. Eley Rideal recombination of hydrogen atoms on Cu(111): Quantitative role of electronic excitation in cross sections and product distributions. *J. Chem. Phys.* **2019**, *150*, 061101.
(78) Jiang, B.; Guo, H. Dynamics in reactions on metal surfaces: A theoretical perspective. *J. Chem. Phys.* **2019**, *150*, 180901.
(79) Wu, Q.; Zhou, L.; Guo, H. Steric Effects in CO Oxidation on Pt(111) by Impinging Oxygen Atoms Lead to an Exclusive Hot Atom Mechansism. *J. Phys. Chem. C* **2019**, *123*, 10509−10516.
(80) Medeiros, P. V. V.; Gueorguiev, G. K.; Stafsröm, S. Benzene, coronene, and circumcoronene adsorbed on gold, and a gold cluster adsorbed on graphene: Structural and Electronic Properties. *Phys. Rev. B: Condens. Matter Mater. Phys.* **2012**, *85*, 205423.
(81) Buimaga-Iarinca, l.; Morari, C. Adsorption of small aromatic molecules on gold: a DFT localized basis set study including van der Waals effects. *Theor. Chem. Acc.* **2014**, *133*, 1502−09.
(82) Lee, J.; Dougherty, D. B.; Yates, J. T. Edge-on Bonding of Benzene Molecules in the Second Adsorbed Layer on Cu(110). *J. Phys. Chem. B* **2006**, *110*, 15645−15649.
(83) Sinnokrot, M. O.; Sheril, C. D. High-Accuracy Quantum Mechanical Studies of π-π Interactions in Benzene Dimers. *J. Phys. Chem. A* **2006**, *110*, 10656−10668.
(84) Tummanapelli, A. K.; Vasudevan, S. Communication: Benzene dimer- The free energy landscape. *J. Chem. Phys.* **2013**, *139*, 201102.
(85) Cruz, M. T.; de M. Carneiro, W. J.; Aranda, D. A. G.; Bühl, M. Density Functional Theory Study of Benzene Adsorption on Small Pd and Pt Clusters. *J. Phys. Chem. C* **2007**, *111*, 11068−11076.

DOI: 10.1021/acs.jpcc.9b08327
J. Phys. Chem. C 2019, 123, 27628−27642